A Tale of Two Disks: Mapping the Milky Way with the Final Data Release of APOGEE

Julie Imig [iD],[1] Cathryn Price,[1] Jon A. Holtzman [iD],[1] Alexander Stone-Martinez [iD],[1] Rachael L. Beaton [iD],[2,3,4]
Timothy C. Beers,[5] Michael R. Blanton [iD],[6] Joel R. Brownstein [iD],[7] Katia Cunha,[8] Diane K. Feuillet [iD],[9]
Sten Hasselquist [iD],[2] Christian R. Hayes [iD],[10] Jennifer A. Johnson [iD],[11] Henrik Jönsson [iD],[12]
Richard R. Lane [iD],[13] Jianhui Lian [iD],[14] Steven R. Majewski [iD],[15] Szabolcs Mészáros [iD],[16,17,18]
David L. Nidever [iD],[19] Annie C. Robin [iD],[20] Matthew Shetrone [iD],[21] Verne Smith [iD],[22] David H. Weinberg [iD],[11,23]
and et al.

[1] *Department of Astronomy, New Mexico State University, P.O.Box 30001, MSC 4500, Las Cruces, NM, 88033, USA*
[2] *Space Telescope Science Institute, 3700 San Martin Drive, Baltimore, MD 21218, USA*
[3] *Department of Astrophysical Sciences, Princeton University, Princeton, NJ 08544, USA*
[4] *The Observatories of the Carnegie Institution for Science, 813 Santa Barbara St., Pasadena, CA 91101*
[5] *Department of Physics and Astronomy and JINA Center for the Evolution of the Elements, University of Notre Dame, Notre Dame, IN 46556, USA*
[6] *Center for Cosmology and Particle Physics, Department of Physics, 726 Broadway, Room 1005, New York University, New York, NY 10003, USA*
[7] *Department of Physics and Astronomy, University of Utah, 115 S. 1400 E., Salt Lake City, UT 84112, USA*
[8] *Steward Observatory, University of Arizona, Tucson, AZ 85721, USA*
[9] *Lund Observatory, Department of Astronomy and Theoretical Physics,
Box 43, SE-221 00 Lund, Sweden*
[10] *NRC Herzberg Astronomy and Astrophysics Research Centre, 5071 West Saanich Road, Victoria, B.C., Canada, V9E 2E7*
[11] *The Department of Astronomy and Center of Cosmology and Astro Particle Physics, The Ohio State University, Columbus, OH 43210, USA*
[12] *Materials Science and Applied Mathematics, Malmö University, SE-205 06 Malmö, Sweden*
[13] *Centro de Investigación en Astronomía, Universidad Bernardo O'Higgins, Avenida Viel 1497, Santiago, Chile*
[14] *Max Planck Institute for Astronomy, 69117, Heidelberg, Germany*
[15] *Department of Astronomy, University of Virginia, Charlottesville, VA 22904, USA*
[16] *ELTE Eötvös Loránd University, Gothard Astrophysical Observatory, 9700 Szombathely, Szent Imre H. st. 112, Hungary*
[17] *MTA-ELTE Lendület "Momentum" Milky Way Research Group, Hungary*
[18] *MTA-ELTE Exoplanet Research Group, Szombathely, Szent Imre h. u. 112., H-9700, Hungary*
[19] *Department of Physics, Montana State University, P.O. Box 173840, Bozeman, MT 59717, USA*
[20] *Institut UTINAM - UMR 6213 - CNRS - University of Bourgogne Franche Comté, France, OSU THETA, 41bis avenue de l'Observatoire, 25000, Besançon, France*
[21] *University of California Observatories, UC Santa Cruz, Santa Cruz, CA 95064*
[22] *NSF's National Optical-Infrared Astronomy Research Laboratory, 950 North Cherry Avenue, Tucson, AZ 85719, USA*
[23] *Institute for Advanced Study, Princeton, NJ 08540, USA*

ABSTRACT

We present new maps of the Milky Way disk showing the distribution of metallicity ([Fe/H]), α-element abundances ([Mg/Fe]), and stellar age, using a sample of 66,414 red giant stars from the final data release (DR17) of the Apache Point Observatory Galactic Evolution Experiment (APOGEE) survey. We measure radial and vertical gradients, quantify the distribution functions for age and metallicity, and explore chemical clock relations across the Milky Way for the low-α disk, high-α disk, and total population independently. The low-α disk shows a negative radial metallicity gradient of -0.066 ± 0.01 dex kpc^{-1}, which flattens with distance from the midplane. The age profile of the low-α disk is flat near the center of the Galaxy, and steeper moving out in radius. The high-α disk has a flat radial gradient in metallicity and age across nearly all locations of the disk. The age and metallicity distribution functions vary with radius and height, notably shifting from negatively-skewed in the inner Galaxy to positively-skewed at large radius. Significant bimodality in the [Mg/Fe]-[Fe/H] plane and in the [Mg/Fe]-age relation persist across the entire disk. These results act as critical constraints on galactic evolution models, further constraining which physical processes played a dominant role in the formation of the Milky Way disk. We discuss how radial migration predicts many of the observed

trends near the solar neighborhood and in the outer disk, but an additional more dramatic evolution history, such as the multi-infall model or a merger event, is needed to explain the chemical and age bimodality in the central Galaxy.

1. INTRODUCTION

The positions, chemical compositions, and ages of individual stars in the Milky Way reflect the formation and evolution history of our Galaxy, with each individual star acting as a "fossil" containing the chemical fingerprint of the interstellar gas from which it formed. Our inside perspective in the Milky Way grants the ability to study it in greater detail than any other galaxy, placing strong observational constraints on formation models and simulations of disk galaxies. For this reason, constraining the chemical and dynamical properties of the stellar populations in the Milky Way disk remains a cornerstone of modern galactic astronomy.

Understanding the present-day chemical structure of our Galaxy has been increasingly successful with the advent of large spectroscopic stellar surveys like APOGEE (Majewski et al. 2017), Gaia (Gaia Collaboration et al. 2021), Gaia-ESO (Gilmore et al. 2022), LAMOST (Luo et al. 2015), GALAH (Buder et al. 2018), and RAVE (Steinmetz et al. 2020). These surveys obtain precise kinematic and chemical information for a combined millions of stars across the Milky Way, with increasing sample sizes and more complete spatial coverage with every generation of survey. When paired with precise distances and positions from Gaia astrometry (Gaia Collaboration et al. 2018, 2021), these large surveys can access the evolution history of a large fraction of the Galactic disk. Even stellar ages, notoriously difficult to infer as they previously could not be directly measured for individual stars, are now readily available through the precise measurements of the masses for thousands of red giant stars available through asteroseismology (e.g., Pinsonneault et al. 2018; Miglio et al. 2021). These asteroseismic data sets are additionally used as training sets for machine learning techniques, expanding the stellar sample with age estimates to hundreds of thousands of stars (e.g., Ness et al. 2016; Leung & Bovy 2018; Mackereth et al. 2019; Wu et al. 2019; Ciucă et al. 2021, Stone-Martinez et al. 2022).

Despite this wealth of data, the debate remains heated around which physical processes played the largest roles in shaping the Milky Way's disk. The structural and chemical distribution of stars in the Milky Way has been well studied, leading to the discovery of two distinct stellar components, the "thin" and "thick" disk near the solar neighborhood (e.g., Yoshii 1982; Gilmore & Reid 1983). These components are distinct in their dynamic signature, with the thick disk characterized by kinematically hotter stellar orbits (larger vertical velocity dispersion), and a slower systemic rotational velocity than the thin disk (e.g., Soubiran et al. 2003; Jurić et al. 2008; Kordopatis et al. 2013; Robin et al. 2017). The thin disk is also generally accepted to be more radially extended, and as the name implies, has a smaller scale height than the thick disk (e.g., Bovy et al. 2012b, 2016; Mackereth et al. 2017; Lian et al. 2022a). The two disks also differ in their chemical fingerprints, with the thin disk generally containing younger metal-rich stars characterized by their lower α-element[1] abundances relative to the older, more metal-poor thick disk (e.g., Fuhrmann 1998; Bensby et al. 2005; Reddy et al. 2006; Lee et al. 2011; Bovy et al. 2012b, 2016; Nidever et al. 2014; Hayden et al. 2015; Mackereth et al. 2017; Vincenzo et al. 2021; Katz et al. 2021). The [Mg/Fe] ratio reflects the relative iron enrichment by prompt, massive core-collapse supernovae compared to the longer timescale Type Ia supernovae. Because of this, the [Mg/Fe] ratio is generally high in populations that formed during rapid and efficient starbursts, and approaches solar "α-poor" values in populations that form steadily over long time periods (e.g., Matteucci & Brocato 1990; Thomas et al. 2005). Thus, the chemical differences between the thin and thick disk suggests that they formed via distinct pathways, leaving the evidence of their enrichment histories within the present-day chemical structure of the Galaxy. However, many of these studies are biased towards the solar neighborhood due to observation limitations, and there has been some debate on whether the

---

[1] α-elements are elements with an atomic number multiple of 4 (the mass of a Helium nucleus, an α-particle), e.g., O, Mg, S, Ca

two components are truly distinct at all (e.g., Bensby et al. 2007; Bovy et al. 2012a; Kawata & Chiappini 2016; Hayden et al. 2017).

Nevertheless, different explanations for the origins of this chemical bimodality in the disk have been proposed, using a combination of physical processes such as star formation, gas accretion, quenching, galaxy mergers, and stellar radial migration to attempt to explain the observed trends. The different models can be generally categorized into two scenarios: the "two-infall" models where the thick disk forms first followed by the thin disk, and the "superposition" models, where the two disks form simultaneously.

The "two-infall" class of models, originally of Chiappini et al. (1997) and Chiappini et al. (2001), describe a scenario wherein the Milky Way first forms from the collapse of primordial gas, creating the progenitor of the present-day thick disk in a fast burst of star formation. The gas reservoir of the Galaxy is then quenched, entering a quiescent period of little star formation until the Galaxy receives a second infall of pristine gas. This accretion of fresh material dilutes the metallicity of the interstellar medium before reigniting star formation that forms the thin disk. The second gas infall happens over a longer time scale, allowing for a period of more continuous star formation, resulting in the α-poor nature of thin disk. Linden et al. (2017) constrained the timing of the second infall to be between 7-8 Gyr ago based on the ages and chemistry of star clusters in APOGEE. Spitoni et al. (2019a, 2020, 2021) expand on this model, constraining the length of the delay between the two episodes of gas infall to be between 3 - 5.5 Gyr, and proposing the second gas infall corresponds to a merger event with a gas-rich dwarf galaxy around 8-11 Gyr ago. This may coincide with the Milky Way's accretion of the Gaia-Enceladus dwarf galaxy, estimated to have happened 10 Gyr ago (Helmi et al. 2018; Vincenzo et al. 2019).

A number of *three*-infall models have also recently been proposed, including the model of Spitoni et al. (2022b) constrained to Gaia data. Their most recent infall starts ~2.7 Gyr ago and gives birth to the recently discovered young, low-α stars that are impoverished in some elements (Gaia Collaboration et al. 2022). This latest infall may be linked with the Sagittarius dwarf spheroidal galaxy's most recent perigalactic passage through the Milky Way's disk (Ruiz-Lara et al. 2020; Laporte et al. 2019; Antoja et al. 2020). A starburst 2-3 Gyr ago has been detected independently in Isern (2019) and Mor et al. (2019).

The works of Lian et al. (2020a,b,c) and Lian et al. (2021) present a modified version of the two-infall model.

In their version, an underlying continuous episode of gas accretion is interrupted by two rapidly quenched starbursts. The first starburst forms the high-α thick disk, and the second starburst forms the metal-poor end of the low-α sequence 6 Gyr later. The metal-rich low-α sequence is attributed to the secular evolution phase between the two bursts.

Another variation of the two-infall model without the inclusion of merger events has been supported by recent chemo-dynamical simulations from Khoperskov et al. (2021). As in previous models, the thick disk is formed early on in a burst of star formation in a turbulent, compact disk. Stellar feedback from the formation of the thick disk drives outflows that quench star formation, enrich the Galactic halo, and eventually, feed the gas back into the disk on a more sustained timescale, creating the thin disk with a "galactic fountain" (e.g., Shapiro & Field 1976; Bregman 1980; Marinacci et al. 2011; Fraternali 2017). The models of Haywood et al. (2016, 2018, 2019) support this scenario, where the high-α population was formed early on in a turbulent gas-rich disk with strong feedback, and the leftover, diluted gas forms the low-α thin disk on longer timescales.

The "superposition" class of chemical evolution models, pioneered by Schönrich & Binney (2009a,b), reproduce the observed disk dichotomy without the need for a violent merger history to heat the thick disk. In this scenario, the chemical locus of the thin disk is not an evolutionary track; it is a superposition of end points of evolutionary tracks from different Galactocentric radii (e.g., Nidever et al. 2014; Kubryk et al. 2015; Sharma et al. 2021a). Stars from these different tracks reach the solar neighborhood by radial migration, a natural consequence of the Galaxy's spiral structure (Sellwood & Binney 2002; Roškar et al. 2008). Stars in the high-α thick disk formed early during an efficient phase of rapid star formation, primarily in the inner Galaxy, before migrating to their present day radial distribution.

This superposition model is expanded on in the works of Minchev et al. (2013, 2014), Minchev et al. (2017), and Johnson et al. (2021), which also emphasize the importance of radial migration in the Milky Way's structure. In these models, gas inflows, outflows, and star formation rates vary with Galactic location, emphasizing the radial dependence of the disk's chemical evolution history. Stellar radial migration allows stars to move around the Galaxy as time progresses, and potentially enrich a different spatial zone than the one they were born in when they die. These models show that this radial migration is the key to reproducing many of the observed trends in the Milky Way, including the

changes of [Mg/Fe] and [Fe/H] distributions with radius and height.

A third, qualitatively different scenario is proposed by the "clumpy formation" model of Clarke et al. (2019), motivated by results from hydrodynamical simulations. In their picture, the low-α thin disk is a true evolutionary sequence corresponding to inefficient star formation, and the high-α population is formed mainly during rapid, clumpy bursts in the Galaxy's early gas rich phase. These clumps are comparable to those observed in high-redshift galaxies with the *Hubble Space Telescope* (e.g., Elmegreen et al. 2005). In addition to the chemical bimodality, these models also reproduce the observed mass density structure of the Milky way, including the flared thin disk (Beraldo e Silva et al. 2020; Amarante et al. 2020).

The discrepancy between these different proposed explanations, that all reasonably reproduce the observed trends in the Milky Way's disk, can only be closed with more observational constraints. Detailed chemical maps which cover the entire span of the disk, robust measurements of the Milky Way's radial and vertical metallicity gradients, and the metallicity distribution function will help constrain which physical processes played an important role in the formation of the disk. Adding in the ages of stars can provide an important axis for interpreting these results, as they enable a direct temporal connection between the properties of individual stars and the evolutionary time scale of the Milky Way (e.g., Mackereth et al. 2017; Feuillet et al. 2019; Vázquez et al. 2022).

In this paper, the final data release of the Apache Point Galactic Evolution Experiment (APOGEE; Majewski et al. 2017; Abdurro'uf et al. 2022) is used to further explore the properties of the Milky Way, with a larger sample size and greater spatial coverage than previously available.

The chemical cartography of the Milky Way has been extensively studied previously using a variety of different surveys including RAVE (e.g, Kordopatis et al. 2013; Robin et al. 2017), GALAH (e.g., Lin et al. 2019; Hayden et al. 2020; Sharma et al. 2021b), LAMOST (e.g., Huang et al. 2020; Vickers et al. 2021; Hawkins 2022), Gaia (e.g., Lemasle et al. 2018; Gaia Collaboration et al. 2022; Poggio et al. 2022), Gaia-ESO (e.g., Bergemann et al. 2014; Magrini et al. 2018; Vázquez et al. 2022), and previous data releases of APOGEE (e.g., Nidever et al. 2014; Hayden et al. 2015; Weinberg et al. 2019; Eilers et al. 2021; Katz et al. 2021). These works, and others, have impressively advanced the field of chemical cartography over the last decade, meaning that many of the results presented in this paper are not new. However, the final data release of APOGEE presents a larger and more detailed base data set than previously available. This allows us to cull a selected high-quality sample, minimizing systematics while still probing a large number of stars at different locations across the Galaxy. Additionally, APOGEE has the distinct advantage of working in the infrared, easily accessing the heavily dust-obscured regions like the Galactic center and mid-plane, which are often beyond the reach of optical surveys.

Our study complements the DR17-based study of Weinberg et al. (2022), which focused on abundance trends of [X/Mg] for many different elements. These trends, which are nearly universal throughout the disk, provide insights on nucleosynthetic processes, while the distribution of stars in [Mg/Fe], [Fe/H], and age across the disk provide constraints on Galactic history.

In this work, we build upon the decades of previous discoveries and explore the chemical trends in the Milky Way disk through the legacy of the APOGEE survey. A high-quality sample of $66,414$ red giant stars and their precise measurements of metallicity ([Fe/H]), ages, and α-element abundances ([Mg/Fe]) are used to create maps, measure gradients, quantify distribution functions, and trace age-abundance relations across the Milky Way disk, and compare the observations with the most recent models. In short, we find evidence supporting both classes of chemical evolution models; Radial migration is an important process in shaping the disk over time, but the observed bimodality in α-element abundances and ages persists even in disk regions where radial migration is not expected to be as prevalent. This suggests a multi-phase star formation history, such as that presented in the two-infall class of models, is at least partially responsible for the formation of the Milky Way as seen today.

Section 2 contains an overview of the APOGEE survey and supplementary data used in this study. Spatial maps, gradient measurements, distribution functions, and other results are presented in Section 3 and compared with previous literature. In Section 4, we discuss our results in the context of chemical evolution models. The conclusions we draw from this study are presented in Section 5.

2. DATA

2.1. *APOGEE*

The Apache Point Observatory Galactic Evolution Experiment (APOGEE; Majewski et al. 2017) is a high-resolution ($R \sim 22,500$) near-infrared ($1.51 - 1.70$ μm) spectroscopic survey containing observations of 657,135 unique stars released as part of the SDSS-IV survey (Blanton et al. 2017). The spectra were obtained us-

ing the APOGEE spectrograph (Wilson et al. 2019) mounted on the 2.5m SDSS telescope (Gunn et al. 2006) at Apache Point Observatory to observe the Northern Hemisphere (APOGEE-N), and expanded to include a second APOGEE spectrograph on the 2.5 m Irénée du Pont telescope (Bowen & Vaughan 1973) at Las Campanas Observatory to observe the Southern Hemisphere (APOGEE-S). The final version of the APOGEE catalog was published in December 2021 as part of the 17th data release of the Sloan Digital Sky Survey (DR17; Abdurro'uf et al. 2022) and is available publicly online through the SDSS Science Archive Server and Catalog Archive Server[2].

The APOGEE data reduction pipeline is described in Nidever et al. (2015). Stellar parameters and chemical abundances in APOGEE were derived within the APOGEE Stellar Parameters and Chemical Abundances Pipeline (ASPCAP; Holtzman et al. 2015; García Pérez et al. 2016; Holtzman et al. 2018; Jönsson et al. 2020, J.A. Holtzman et al. 2022 in prep.). ASPCAP derives stellar atmospheric parameters, radial velocities, and as many as 20 individual elemental abundances for each APOGEE spectrum by comparing each to a multi-dimensional grid of theoretical model spectra (Mészáros et al. 2012; Zamora et al. 2015) and corresponding line lists (Shetrone et al. 2015; Smith et al. 2021), employing a χ^2 minimization routine with the code `FERRE` (Allende Prieto et al. 2006) to derive the best-fit parameters for each spectrum. We highlight that several elements (notably [Mg/Fe]) were updated in DR17 to include non-LTE effects in the stellar atmosphere. ASPCAP reports typical precision in metallicity measurements within 0.01 dex (Jönsson et al. 2018). In this study, we adopt the calibrated values for surface gravity (log g), metallicity ([Fe/H]), and α-element abundances ([Mg/Fe]) from ASPCAP. We adopt [Mg/Fe] for our α-element abundance instead of the "total" [α/M], because [Mg/Fe] is the most precisely measured abundance by ASPCAP, and this element ratio has been traditionally used to define the boundary between the chemical thin and thick disk.

2.2. Sample Selection

Several cuts were made to the full APOGEE catalog to refine our sample. First, only stars defined as APOGEE main survey targets (also sometimes called the "main red giant sample") were selected using the `EXTRATARG` flag. This removes any duplicate entries, as well as any ancillary science or other survey stars that were targeted
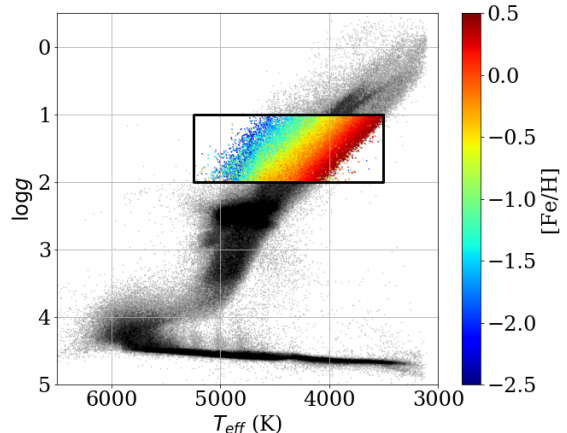
Figure 1. The T_{eff}-log g distribution of stars in the sample described in Section 2. Our adopted red giant sample is outlined in black and plotted by color (metallicity), while the full APOGEE sample is shown in gray in the background for reference.

for observation for a specific purpose (e.g., satellite or dwarf galaxy targets, star cluster member candidates, *Kepler* Objects of Interest). The main survey targets were randomly selected for observation from the 2MASS catalog, based on their $(J-K)$ color and H-band apparent magnitude. For more information on the targeting strategies of APOGEE, see Zasowski et al. (2013, 2017), Beaton et al. (2021), and Santana et al. (2021).

Stars with noisy spectra ($S/N < 50$) or unreliable parameter estimates from ASPCAP were removed from our sample using the `SN_BAD` and `STAR_BAD` ASPCAP bits respectively. The latter is triggered when the derived parameters for a star are designated a bad fit by its high χ^2 value, when the derived temperature does not match the star's observed color, when any individual stellar parameter measurement is flagged as bad, or when the derived parameters lie on an edge of the synthetic spectral grid.

The sample is further restricted to stars with surface gravity values between $1 \leq \log g \leq 2$. Limiting to a small range in log g minimizes potential systematic uncertainties in abundance measurements, which tend to present as a function across T_{eff} and log g in APOGEE (e.g., Jönsson et al. 2018; Eilers et al. 2021). The higher luminosity of these giants helps probe larger distances, allowing for a wide range of positions to be sampled across the Galactic disk in our study. Fainter stars may be better sampled closer to the Sun, but to keep our sample consistent across all distances, we apply this log g cut to ensure the trends we are documenting are not attributed to any systematic bias. Eilers et al. (2021)

presents an empirical correction for these systematics for those interested; this would mainly be a concern if the expected distribution of $\log g$ in observations varies significantly with distance, which we do not expect in our sample. The lower $\log g$ limit is also imposed by the availability of asteroseismic data, as no age estimates are available for stars with $\log g < 1$ by our techniques.

Figure 1 shows the $T_{\rm eff}$-$\log g$ distribution of the sample after these refinements. The final number of stars in our RGB sample is 66,414. Due to the particulars of APOGEE field selection, there are more stars above the disk ($Z \geq 0; N = 37,941$) than below ($Z \leq 0; N = 28,473$), and more observations towards the Galactic center ($R \leq R_{\odot}; N = 35,454$) than outward ($R \geq R_{\odot}; N = 30,960$). The spatial distribution of our sample is shown in Figure 2. The stellar distance estimates used for this Figure (and the remaining of the paper) are described in Section 2.4.

In this work, we make no correction for the selection biases within the APOGEE survey. Stars close to the solar neighborhood will be over-represented in our sample. As shown in Figure 2, as distance from the Sun increases, the number of stars available in the APOGEE sample decreases.[3] There are certain limitations that this selection function imposes on this work and similar studies. Specifically, results should not be averaged over a large spatial range, as the relative number of observed stars will clearly weight the average towards the solar neighborhood. Additionally, nothing can be inferred from the relative number of stars between locations, or about the intrinsic density profile of stars in the disk, because the former is so heavily influenced by the selection function. That said, the effect should be negligible when confined within a small spatial zone and $\log g$ limit in the Galaxy, such that general abundance trends and *normalized* number distributions should be consistent even without correcting for the APOGEE selection function (e.g., Hayden et al. 2015, Appendix A). In this work, we consistently bin stars in different ranges of R and Z to avoid this bias and explore how chemical and age trends vary across the disk. A more complete prescription on how to account for the effects of the selection function in APOGEE has been published in Bovy et al. (2012b, 2016), Mackereth et al. (2017) for previous data releases, and Imig et al. (in prep.)
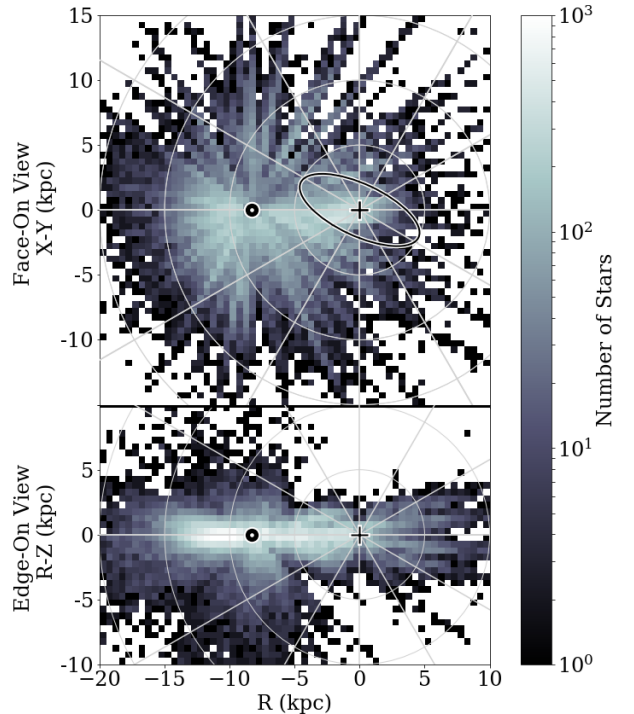
Figure 2. The spatial distribution of stars in our sample shown as a face-on view of the Galaxy (X-Y plane; top panel), and an edge-on view (R-Z plane; bottom panel). Each spatial bin of $\Delta X = \Delta Y = \Delta Z = 0.5$ kpc is colored by the number of stars in that location. The position of the Sun at $X = -8.3$ kpc is denoted by the solar symbol ($\odot$), and the Galactic center is marked with a plus ($+$). The ellipse around the Galactic center marks the approximate location of the bar, as an ellipse with major axis length 10 kpc, a 0.4 axis ratio, and rotated $25°$.

for DR17. Imig et al. (in prep.) will also present the density distribution of mono-age mono-abundance stellar populations in APOGEE DR17 after correcting for the selection function.

2.3. *[Mg/Fe] Subsamples*

In Figure 3, we show the [Mg/Fe]-[Fe/H] plane for our full sample, where the bimodal distribution in [Mg/Fe] is obvious (e.g., Fuhrmann 1998; Bensby et al. 2005; Reddy et al. 2006; Lee et al. 2011; Hayden et al. 2015; Katz et al. 2021). Although there is some debate on whether the two sequences are truly distinct (see Introduction), we use this figure to define two further subsamples in our data to investigate this question later. Vincenzo et al. (2021) demonstrate that the distribution in [Mg/Fe] at fixed [Fe/H] is genuinely bimodal when
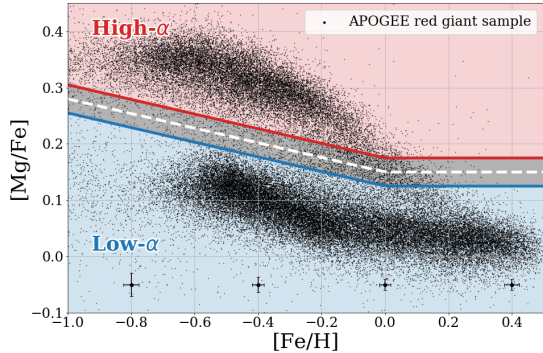
Figure 3. The [Mg/Fe]-[Fe/H] plane for stars in our red giant sample (black points), demonstrating the adopted definition of the low-α (blue) and high-α (red) sequence defined in Equation 1. The gray region is an added buffer zone of [Fe/H]=$\pm$0.025 dex around the line to remove overlap between the two sequences due to abundance uncertainties. The typical uncertainties associated with each measurement of [Fe/H] and [Mg/Fe] are shown in the error bars near the bottom of the plot (as the $\pm 2\sigma$ value), for several selected metallicities.

considering the full disk population at near-solar radii, after accounting for the APOGEE selection function. We define the alpha-poor "thin disk" sequence and the α-rich "thick disk" sequence by splitting the full sample into two groups defined by an arbitrary line in [Mg/Fe]-[Fe/H] space, shown in Figure 3. We adopt a similar limit as Weinberg et al. (2022) parameterized by the equation:

$$[Mg/Fe] = \begin{cases} 0.15 - 0.13 * [Fe/H] & \text{if } [Fe/H] \leq 0 \\ 0.15 & \text{if } [Fe/H] > 0 \end{cases} \quad (1)$$

This separation in α-element abundances is shown in Figure 3. A conservative buffer zone within $\pm$0.025 dex of the line is excluded to remove potential overlap between the two sequences. This value is reasonably larger than the typical uncertainties of APOGEE abundance measurements, shown as the $\pm 2\sigma$ (or 95% confidence interval) in the error bars across the bottom of the plot.

2.4. Age and Distance Estimates

Accurately mapping the Milky Way in three dimensions requires knowing precise distances to every star in our sample. Galactocentric positions were calculated for each star using the right ascension (RA) and declination (DEC) from APOGEE observations and distance estimates from the APOGEE `distmass` value added cat-
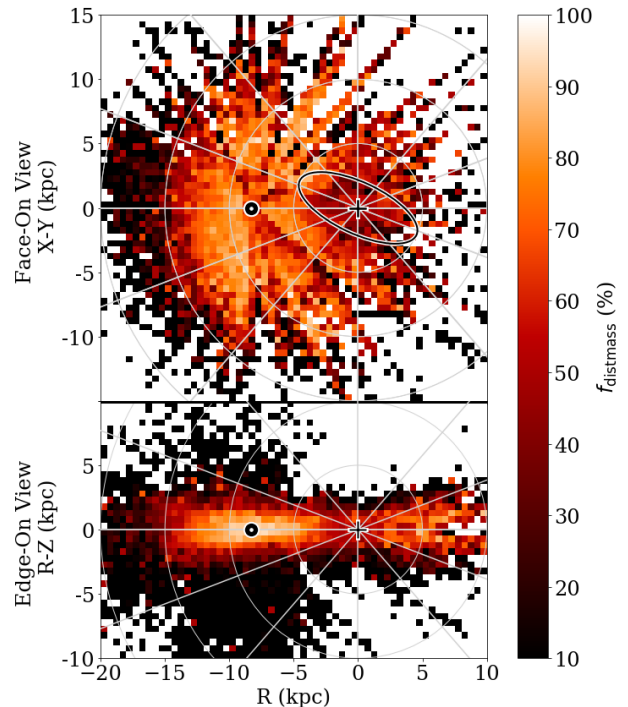
Figure 4. The same as Figure 2, but colored by the fraction of stars in our sample that survive the additional distmass quality cuts described in Section 2.4. The purpose of this figure is to qualitatively explore how the distmass criterion might later bias our results using stellar age estimates; see 2.4 for more detail.

alog (A. Stone-Martinez et al. 2022, submitted).[4] The `distmass` distances were obtained through a neural network that was trained to estimate a star's luminosity based on its ASPCAP parameters, using Gaia and cluster distances to provide the training labels. Distance estimates from the `distmass` catalog are typically precise within 10%. For the purpose of calculating Galactocentric coordinates, we define the reference location of the Sun to be $R_\odot = 8.3$ kpc with a height of $z_\odot = 0.027$ kpc above the plane (Bland-Hawthorn & Gerhard 2016).

For evolved red giant stars, carbon and nitrogen abundances provide mass information because of the mass-dependence of stellar mixing, allowing the determination of stellar masses for stars without asteroseismology. This fundamental property is used to derive stellar age estimates in the `distmass` catalog, wherein ages are derived by training a second neural network on the ASPCAP parameters of stars with asteroseismology masses from the APOGEE-*Kepler* overlap survey (APOKASC; Pinsonneault et al. 2018). The neural network learns the relations between the ASPCAP parameters and astero-

---

[4] distmass VAC link here

seismic masses for stars from APOKASC, then it predicts the masses for all giant stars from DR17. Knowing the masses for evolved stars, ages can be derived through stellar evolution theory which predicts a star's location on an isochrone. In our technique, isochrones from Choi et al. (2016) were adopted to make this conversion from derived mass to stellar age. Age estimates from the `distmass` catalog are reported to be precise within $\pm 0.14 \log_{10}(\text{age})$ for a $1 M_\odot$ star and $\pm 0.09 \log_{10}(\text{age})$ for a $2 M_\odot$ star.

When using the stellar age estimates, an additional quality flag from the `distmass` catalog is used. Namely, we remove stars that have bit 2 set, indicating stellar parameters T_{eff}, [Fe/H], and $\log g$ lie outside of the range covered by the APOKASC training set; this removes stars with potentially unreliable mass (and therefore age) estimates. For anything involving ages, the full RGB sample is additionally restricted to 42,795 stars with this cut. Notably, all stars with [Fe/H] ≤ -0.5 dex are excluded by this criterion. Metal-poor stars have extra mixing that was not learned by the neural network because there were no metal poor stars in the training set. Because metal-poor stars tend to be older, this means that for age related figures, the oldest stars (age $> 10^{10}$ years) may not be well-represented in our sample; particularly at large radii in the Galaxy.

We qualitatively explore where this may influence our stellar age-related results in Figure 4, which shows the fraction of stars f_{distmass} in every spatial bin ($\Delta X = \Delta Y = \Delta Z = 0.5 kpc$) which survive this additional `distmass` quality cut. Close to the solar neighborhood, the majority of stars pass this additional selection criterion ($f_{\text{distmass}} > 80\%$). Near the center of the Galaxy ($R \leq 5$ kpc), f_{distmass} is generally lower but still exceeds 50%. Beyond $R > 15$ kpc, where most of the stars are expected to be metal-poor, there is a sharp drop in f_{distmass}, regularly reaching fractions lower than $< 20\%$. This shows that our sample with `distmass` ages does not equally represent the full sample everywhere in the Galaxy. Particularly beyond $R > 15 kpc$ we caution against directly comparing our results including age to those made with the full sample. Again, we emphasize that this only impacts our figures which include stellar age.

3. RESULTS

3.1. *Cartography*

Maps of the Galactic disk as a function of [Fe/H], [Mg/Fe], and stellar age are shown in Figure 5 in face-on ($X - Y$ plane; top row) and edge-on ($R - Z$ plane; bottom row) perspectives. The median value of each parameter is calculated for different spatial bins sized

$\Delta X = \Delta Y = 0.5$ kpc, and shown as the respective color on the figure. For the edge-on perspective, the sign of the X coordinate is applied to the R coordinate, to better highlight the spatial coverage of the observations on the opposite side of the Galaxy.

In median metallicity (left column), clear radial and vertical metallicity gradients are visible in the disk, with higher average metallicities near the Galactic center that decline towards outer radii. In median α-element abundances (middle column), the bimodality in the disk shows low-α stars congregating in the "thin disk" near the Galactic midplane, and high-α stars populating the "thick disk" at higher Z locations. At larger radii, the low-α stars extend further above and below the plane. The high-α stars are more centrally concentrated. The right column, colored by median stellar age, contains fewer stars due to the additional cuts described in Section 2.4 when dealing with ages from the `distmass` catalog. Once again, radial and vertical gradients appear in these maps, as well as younger stars extending farther above the plane in the outer Galaxy. The ermost structural features of the Galaxy, such as the bar (noted by the ellipse) and bulge stand out as metal-rich, alpha-poor, and older-aged than stars at similar radii but different azimuthal angles, consistent with previous studies of the central regions of the Galaxy (Wegg et al. 2019; Zasowski et al. 2019; Hasselquist et al. 2020; Eilers et al. 2021; Lian et al. 2021; Queiroz et al. 2021) for this metallicity range.

Dividing the maps into vertical bins reveals more nuanced structure; Figure 6 depicts face-on metallicity maps divided by height above the Galactic plane, from closest to the Galactic plane (top panel; $|Z| \leq 0.5$ kpc) to farthest away (bottom panel; $1 \leq |Z| \leq 2$ kpc). The metallicity gradient is strongest close to the Galactic plane, with locations near the Galactic center showing a higher median metallicity than those at larger radii, as expected. Farther above the mid plane, the trend becomes less apparent, with almost no obvious gradient present when $|Z| \geq 1$ kpc, and the stellar populations showing a lower median metallicity overall. The middle panel ($0.5 \leq |Z| \leq 1$ kpc) shows a peculiar trend where the median metallicity actually increases from $R = 0$ until $R \sim 7$ kpc, and then decreases with a shallow metallicity gradient. This build-up of metal-rich stars in the center of the Galaxy is possibly the signature of the bulge.

The age distribution of the Galactic disk is shown in Figure 7. Again, the age gradient is strong close to the Galactic plane, with older stars more common near the center and younger stars dominating in the outer Galaxy. Unlike in metallicity, there is still a radial age
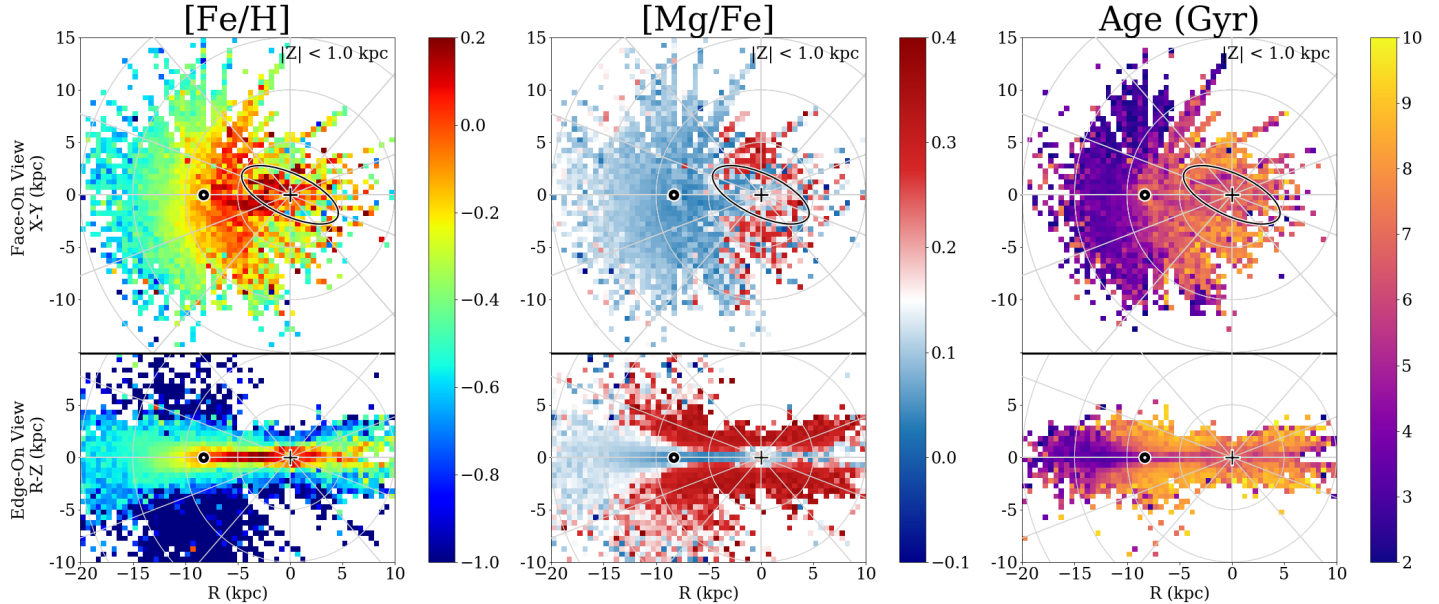
Figure 5. Global Maps of the Milky Way, showing the average distribution of [Fe/H] (left), [Mg/Fe] (middle), and stellar age (right) across the Galaxy. The top row of panels shows a face-on view ($X - Y$ plane), integrated through the disk with $|Z| \leq 1.0$ kpc. The bottom row of panels shows an edge-on view ($R - Z$ plane, with R preserving the sign of X to show the opposite side of the Galaxy), integrated through the whole disk. Colors encode the median quantities in each or $X - Y$ or $R - Z$ pixel. In the face-on views, the age and metallicity gradients are visible, with the Galactic bar standing out as metal-rich and α-poor. The location of the Sun at $X = -8.3$ kpc is denoted by the solar symbol ($\odot$), and the Galactic center is marked with a plus ($+$). The approximate location of the Galactic bar is also shown as an ellipse with major axis length 10 kpc, a 0.4 axis ratio, and rotated $25°$.

gradient above the Galactic plane ($|Z| > 1$ kpc), although in general the stars found above the plane are older than the stars found in the plane.

3.2. [Mg/Fe] Distribution

Figure 8 shows the Galactic distribution of stars in the [Mg/Fe]-[Fe/H] chemistry plane as a function of Galactic position. The different rows are the same vertical bins adopted in previous sections, with the bottom row closest to the Galactic plane ($0 < |Z| < 0.5$ kpc) and the top row farthest from the plane ($1.0 < |Z| < 2.0$ kpc). The columns are different radial bins, from closest to the disk center (left column) to farthest out (right column). Each panel shows the [Mg/Fe]-[Fe/H] distribution of stars in its respective spatial zone, colored by stellar point density (in Figure 8) and stellar age (in Figure 9). Our adopted definition of the split between the high- and low-α sequences (equation 1) is plotted in black. For reference, the gray background highlights the distribution of the full sample, indicating the contour within which 90% of the sample is found.

Generally, the low-α sequence is concentrated close to the Galactic plane (bottom row), and the high-α sequence is more prominent outside the plane (top row)

for $R < 12$ kpc. The location of the high-α sequence does not change based on location in the Galaxy. The low-α sequence is more metal rich near the center of the Galaxy (left column), and moves to more metal-poor with increasing radius (right column). Additionally, at large radii, the low-α sequence extends further above the plane than it does close to the Galactic center. All of this has been well-documented in previous studies (e.g., Bensby et al. 2005; Nidever et al. 2014; Hayden et al. 2015; Katz et al. 2021; Vincenzo et al. 2021; Gaia Collaboration et al. 2022).

Figure 9 shows the spatial distribution of [Mg/Fe] coded by stellar age. The high-α sequence is composed of older stars at all radial bins. The low-α sequence includes older stars close to the Galactic center ($R < 6$ kpc) and younger stars further out in radius. At any radius, the lower [Mg/Fe] stars within the low-α sequence have younger ages.

To aid in the direct comparison between the radial and height bins, Figure 10 shows the contours (top panel) and median (bottom panel) in the [Mg/Fe]-[Fe/H] plane for both the low-α and high-α samples as a function of Galactic radius. In this Figure, the data are restricted
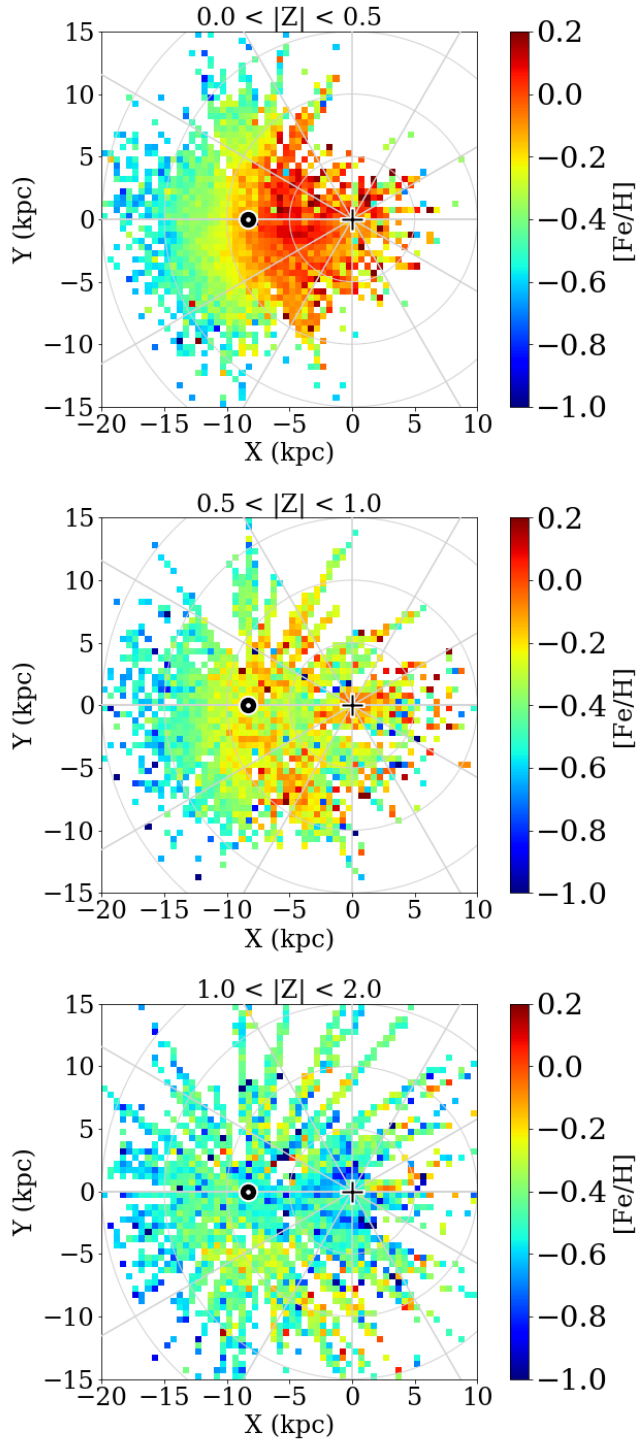
Figure 6. Face-on maps of Galactic disk, showing the median metallicity ([Fe/H]) of stars in spatial bins of $\Delta X = \Delta Y = 0.5$ kpc. The different panels are slices in vertical space, from closest to the Galactic plane (top panel; $|Z| < 0.5$ kpc) to increasing heights above the plane (bottom panel; $1 < |Z| < 2$ kpc). The Sun's position is marked by the solar symbol ($\odot$), and the position of the Galactic center is indicated by a plus ($+$).
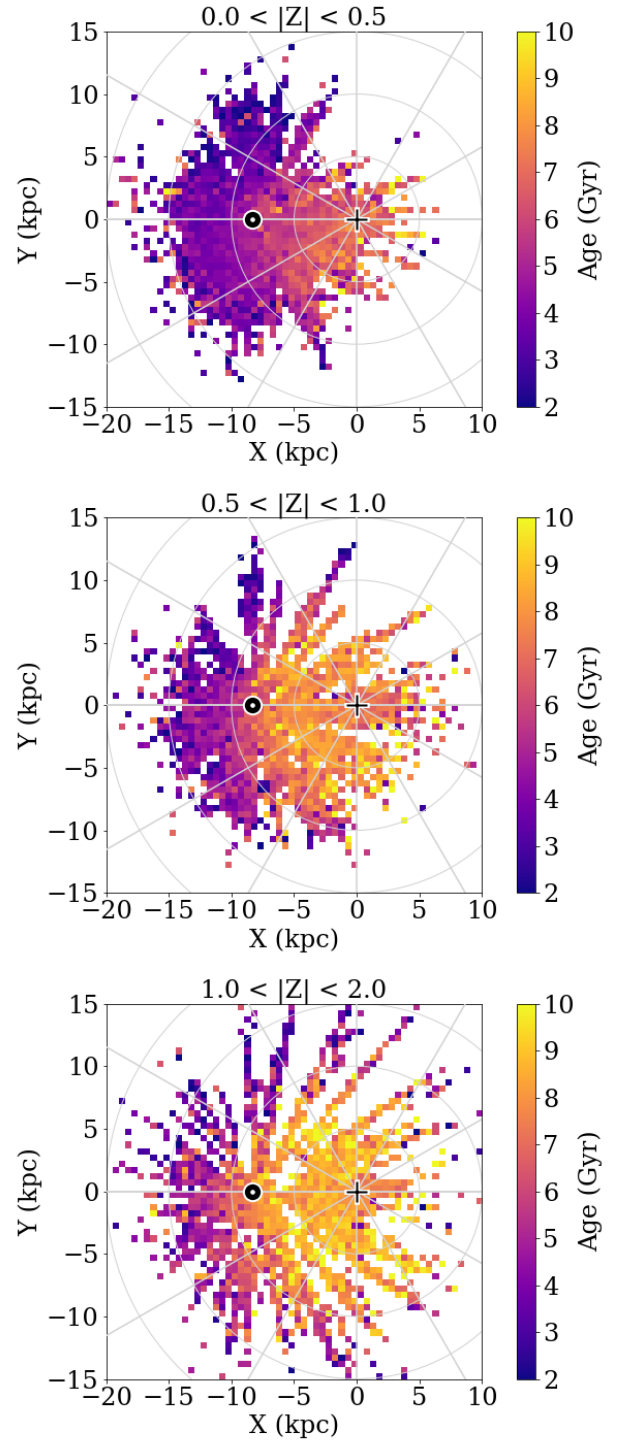
Figure 7. Same as Figure 6, but colored by the median age (in Gyr) of stars in each spatial bins of $\Delta X = \Delta Y = 0.5$ kpc.
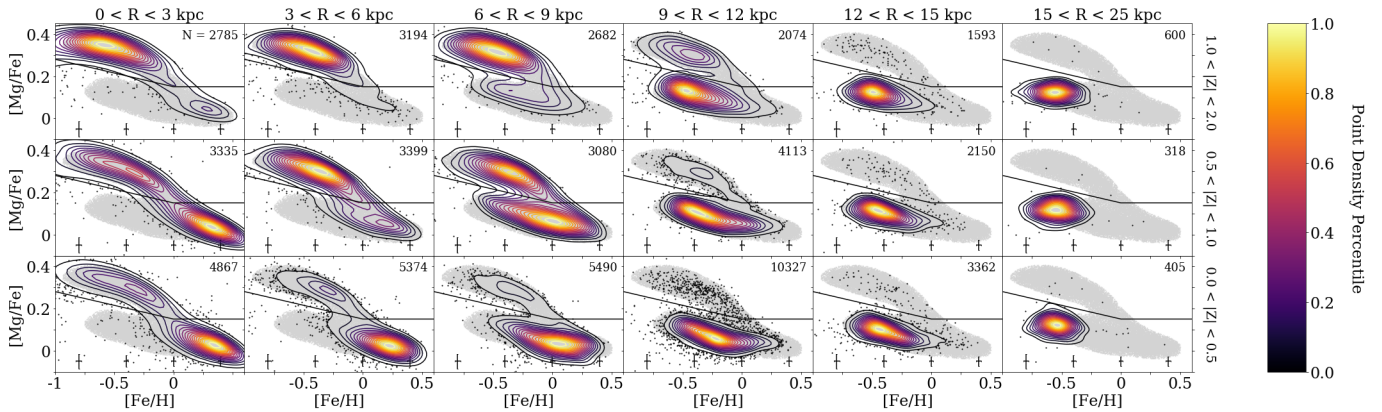
Figure 8. The distribution of stars in the [Mg/Fe] vs. [Fe/H] plane as a function of R and $|Z|$, as a contour map of point density. Spatial bins move from closest to the Galactic plane (bottom row, $0.0 < |Z| < 0.5$ kpc) to farthest above the Galactic plane (top row, $1.0 < |Z| < 2.0$ kpc), and from close to the Galactic center (left column, $0.0 < |R| < 3.0$ kpc) to farthest out in the disk (right column, $15.0 < |R| < 25.0$ kpc). The number in the top-right corner of each panel is the number of stars in our sample in that spatial bin. For reference, the gray background shape and black line is the same in each panel, to highlight how the sequence changes across location in the Galaxy. The black line is the boundary between high- and low-α populations defined in Equation 1, and the gray shape is the contour containing 90% of the points in the full sample. The typical uncertainties in abundance measurements as a function of metallicity are shown as a 2σ value at the bottom of each panel for reference.
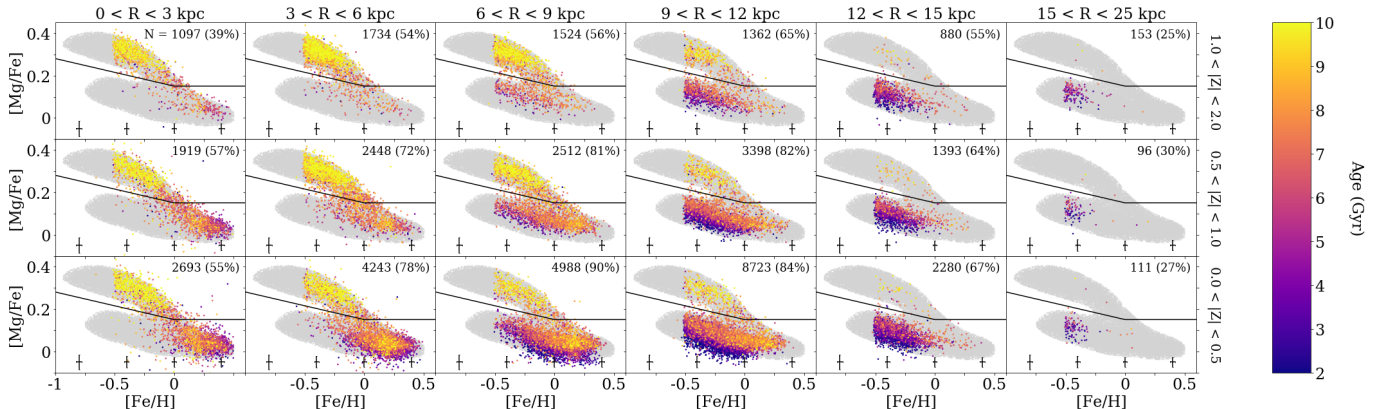

Figure 9. Same as Figure 8, but colored by stellar age. Points with [Fe/H]$\leq$ 0.5 dex have been excluded for potentially unreliable age estimates with the cuts described in Section 2.4. The percentage of stars ($f_{\rm distmass}$) in each bin which pass the distmass quality criterion is shown in parentheses in the upper right corner of each panel.

to the plane ($|Z| < 0.5$ kpc), equivalent to the bottom row in Figures 8 and 9. The contour containing 90% of points in both the low-α and high-α samples is shown in the top panel. The low-α sequence is more metal-rich near the center of the Galaxy, and shifts continuously to lower metallicities and higher-α moving outwards in radius. The high-α sequence's contour is generally the same shape and position at all radii, although close to the center of the Galaxy, the shape extends further to the metal-poor end. In the bottom panel, the median [Mg/Fe] as a function of metallicity is shown for both samples. As before, the low-α sample shifts more metal-poor with increasing radius. The high-α sequence moves slightly downwards (towards more α-poor) with increasing radius. This is also seen in Katz et al. (2021) with

APOGEE data, using the mode of the data, although they find a larger shift of ~ 0.05 dex between the inner and outer Galaxy, while ours is closer to half that at ~ 0.025 dex.

3.3. *Azimuthal Variance in Metallicity*

The degree to which trends in the Galactic disk are azimuthally symmetric has the potential to provide interesting insight into the history of the disk. The stellar distribution across the Galaxy is not uniform, with in-situ non-axisymmetric features such as the Galactic bar and spiral arms containing higher stellar density than surrounding populations, particularly for young stars (e.g., Bland-Hawthorn & Gerhard 2016; Reid et al. 2019; Khoperskov et al. 2020a). Additionally, chemical en-
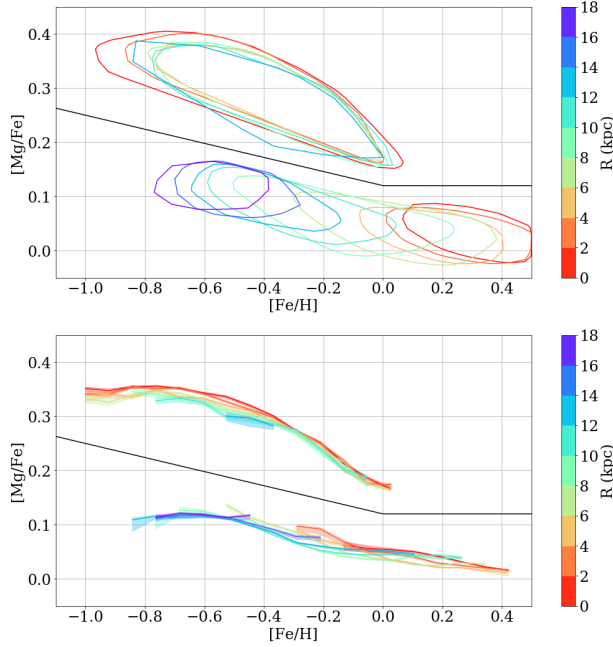
Figure 10. Variation in the [Mg/Fe]-[Fe/H] plane as a function of Galactic radius (color) for stars within $|Z| < 0.5$ kpc of the plane. **Top Panel:** The contour containing 75% of points for both the low-α and high-α samples, calculated separately. **Bottom Panel:** The median [Mg/Fe] as a function of [Fe/H] for both sequences. The shaded regions denotes the $\pm 1\sigma$ uncertainty in the median. In both panels, the black line is our defined boundary between the low-α and high-α described in Equation 1.

richment is strongly dependent on local conditions, and spiral density fluctuations can lead to measurable differences in a galaxy's enrichment history across azimuth (Spitoni et al. 2019b).

To look more closely at the azimuthal symmetry of the disk, the right column of Figure 11 is a metallicity map of the disk identical to Figure 6 but displayed in polar coordinates. The spatial bins are sized $\Delta R = 1$ kpc and $\Delta \theta = 10°$. Like before, the stars are separated into rows based on their height above the Galactic plane. The corresponding panels to the left trace the median metallicity at each radius (y-axis) for different bins in azimuthal angle θ (point color), restricted to $130 \leq \theta \leq 230$ deg, where there is reasonable coverage with radius. At each radius, the expected spread based on uncertainty of the median measurements is shown as the gray shaded region. The expected spread ($\sigma_{[\text{Fe/H}]}$) is defined for a given radius as the sum of the uncertainty in the median for each individual θ bin ($\sigma_{[\text{Fe/H}]}(R, \theta)$), divided by the number of bins with valid data ($N_{bins,\theta}$), whereas the uncertainty in the median for a given az-

imuth bin is the standard deviation in [Fe/H] divided by the square root of the number of stars in that bin:

$$\sigma_{[\text{Fe/H}]}(R)^2 = \frac{1}{N_{bins,\theta}} \sum_{\theta=0}^{360} \sigma_{[\text{Fe/H}]}(R, \theta)^2 \qquad (2)$$

$$\sigma_{[\text{Fe/H}]}(R, \theta)^2 = \frac{1}{N_{stars}} \sum_{i=0}^{N_{stars}} |([\text{Fe/H}]_i - \overline{[\text{Fe/H}]})|^2 \quad (3)$$

Close to the Galactic plane (top row), the outer Galaxy has little metallicity variation across azimuth, although it also has a smaller region of azimuth covered by the observations. Closer to the center of the Galaxy, the median metallicity varies more with azimuthal angle θ, with the spread possibly slightly exceeding the expected uncertainty. In the middle row, a similar trend is seen, where there is more spread with metallicity in azimuth near the center of the Galaxy. There does seem to be an asymmetry in the disk that follows the approximate location of the Galactic bar in these coordinates, with metal-rich stars preferentially residing in the Galactic bar. Higher above the Galactic plane, the variation in azimuth can be attributed entirely to noise from low-number statistics, where the observed spread is all comparable or smaller than the expected spread.

Interactions with satellite galaxies and merger events can also perturb the disk in non-axisymmetric ways, such as warping the disk or introducing kinematic oscillations (e.g., Amôres et al. 2017; Cheng et al. 2020; Chrobáková et al. 2022). The restorative force from these perturbations is weaker in the outer Galaxy, so the presence of these features is generally expected to be more obvious at large radii. We find no significant azimuthal asymmetries in metallicity in the outer disk, but as radius increases, our sample covers less range in θ. As such, we are unable to draw any conclusions on the Milky Way's merger history from these metallicity maps alone.

Recent work has detected azimuthal variations in both the gas phase metallicity (Wenger et al. 2019) and stellar metallicity(Inno et al. 2019; Poggio et al. 2022; Hawkins 2022) possibly corresponding to the Milky Way's spiral arms. Measuring the radial metallicity gradient using Gaia data, Poggio et al. (2022) and Hawkins (2022) report azimuthal variation in the slope on the order of $0.02 - 0.1$ dex kpc^{-1}. If we measure the slope of the profiles in the left column of Figure 11 as a function of azimuthal angle θ, our maximum difference between slopes for the vertical bin closest to the disk is 0.026, which is comparable to the lower end of the variation reported by Poggio et al. (2022), but may not be significant given the uncertainties in our data.
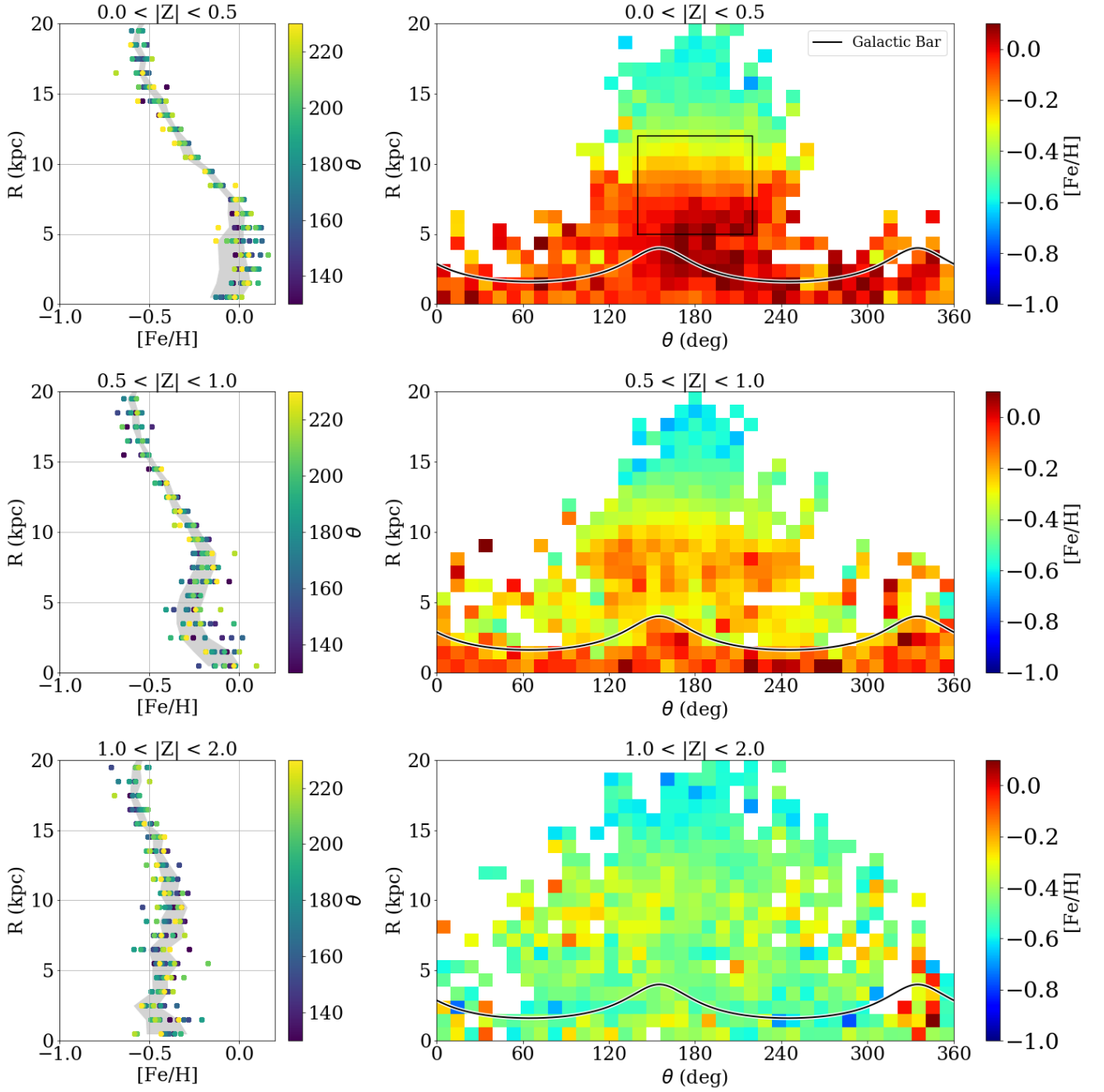
Figure 11. Maps of the median metallicity in the disk in polar coordinates, to highlight any non-axisymmetric features in the disk. The spatial bins are sized $\Delta R = 1$ kpc and $\Delta \theta = 10°$. The rows are different slices in Z, moving from closest to the Galactic plane (top row, $|Z| \leq 0.5$ kpc), to farther above (bottom row, $1 \leq |Z| \leq 2.0$ kpc). The left column shows the median [Fe/H] for each bin as a function of θ (point color), compared to the $\pm 1\sigma$ expected spread from uncertainty in the measurement of the median (gray shaded region). The right column shows the median metallicity maps as a function of radius R and azimuthal angle θ. The black line is the approximate location of the Galactic Bar, defined as an ellipse with major axis length 10 kpc, a 0.4 axis ratio, and rotated 25 degrees. The black square in the top panel highlights the region shown in more detail in Figure 12.
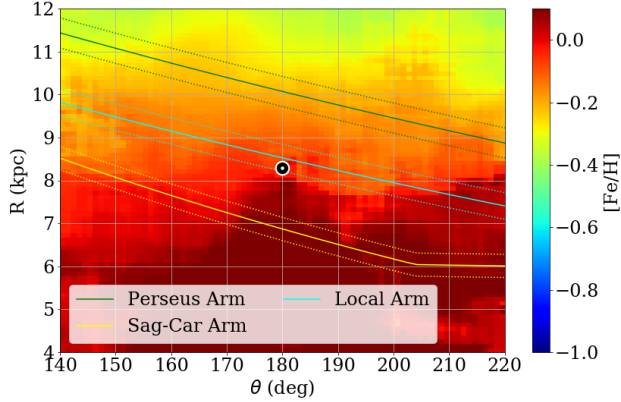
Figure 12. Azimuthal variation in metallicity restricted to a window near the solar neighborhood, outlined by the black rectangle in Figure 11. The metallicity value is calculated as a running median for bin size $\Delta R = 0.5$ kpc and $\Delta\theta = 5°$, evaluated every $\Delta R = 0.1$ kpc and $\Delta\theta = 1°$ for smoothing. The approximate location the nearby spiral arms from Reid et al. (2019) are plotted as colored lines.

In Figure 12, we zoom into a region in the solar neighborhood, where the sample has higher number of stars making it possible to study the chemical distribution in more detail. The exact window used is outlined as the black rectangle in the top-right panel of Figure 11 for reference. Here, the spatial bins are sized $\Delta R = 0.5$ kpc and $\Delta\theta = 5°$ (half the size of the bins in Figure 11), but calculated on a frequency of $\Delta R = 0.1$ kpc and $\Delta\theta = 1°$ as a running median for smoothing. The approximate location of the nearby spiral arms from Reid et al. (2019) are plotted as colored lines. There does seem to be a bit of coherent structure signifying that the median metallicity is not symmetric in azimuth, but it does not obviously follow the spiral arms.

3.4. *Radial and Vertical Metallicity Gradients*

The radial and vertical metallicity gradients in the Milky Way disk have been well-documented observationally, with stars near the center of the Galaxy exhibiting higher metallicity than those at large radii and higher Z (e.g., Hartkopf & Yoss 1982; Cheng et al. 2012; Carrell et al. 2012; Anders et al. 2014; Schlesinger et al. 2014; Hayden et al. 2014; Frankel et al. 2019; Katz et al. 2021; Gaia Collaboration et al. 2022). Such a trend is predicted by "inside out" disk formation models, where stars in the central regions of the Galaxy form earlier on in the Galaxy's history, and the disk subsequently grows outward over time, the global star formation rate consistently decreasing with radius (e.g., Eggen et al. 1962; Larson 1976; Matteucci & Francois 1989; Kobayashi & Nakasato 2011; Minchev et al. 2015). However, ra-
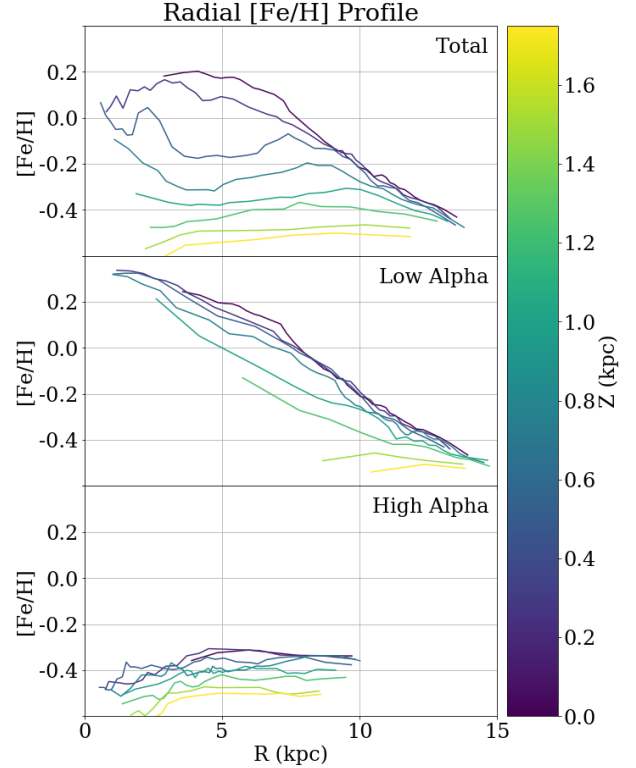
Figure 13. Radial median metallicity profile as a function of height out of the plane (line color), for the total stellar population (top panel), the low-α disk (middle panel), and the high-α disk (bottom panel).
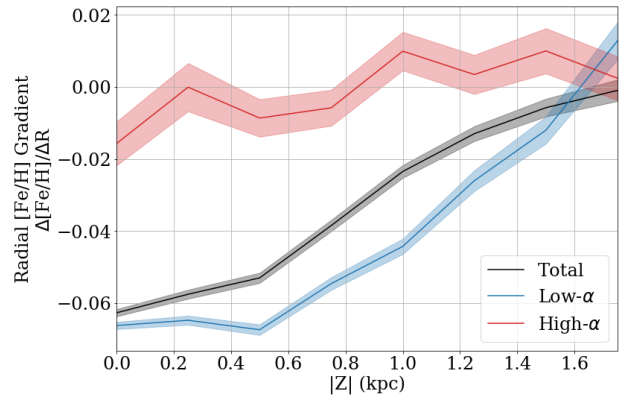
Figure 14. The best-fit slope for each radial metallicity profile in Figure 13 in units of dex kpc^{-1}, fit with a single line for stars beyond $R > 7$ kpc for the total sample (black line), and the low-α (blue line) and high-α (red line) samples independently. The shaded region indicates the $\pm 1\sigma$ uncertainty in the slope measurement.

dial migration could complicate this interpretation because it flattens gradients over time as stars move away from their birth location (e.g., Sellwood & Binney 2002; Roškar et al. 2008; Wang & Zhao 2013; Hayden et al. 2015; Mackereth et al. 2017; Frankel et al. 2018, 2020;

Vickers et al. 2021; Lian et al. 2022b). Without radial migration, gradients are predicted to steepen with time, with the oldest stars having the steepest slope and being more centrally concentrated as a result of the inside-out growth of the Galaxy (e.g., Matteucci & Francois 1989; Bird et al. 2013; Pilkington & Gibson 2012; Gibson et al. 2013; Mollá et al. 2018). Radially dependent outflow efficiencies can also have strong impact on the radial gradients (Johnson et al. 2021), as can radial gas flows within the disk (e.g., Bilitewski & Schönrich 2012).

We measure the median metallicity profile for the disk by first separating stars into bins of Z, and then calculating a running median [Fe/H] for each bin of $N = 200$ data points with an overlap of 50%, sorted by Galactocentric radii. We do this for the total stellar population and repeat the analysis for the high-α and low-α samples described in Section 2.2 separately. The resulting radial median metallicity profiles are shown in Figure 13.

The total sample (Fig. 13 top row) shows a negative metallicity gradient close to the Galactic plane, which flattens out at small radii. Moving above the plane, the slope of the gradient flattens until it becomes slightly positive at $|Z| > 1.6$ kpc.

The low-α disk (Fig. 13 middle row) shows a steep metallicity gradient everywhere, notably missing the flattening in the inner Galaxy seen in the total population. The low-α disk's metallicity gradient flattens with height Z much like the total population.

The high-α disk (Fig. 13 bottom row) exhibits a much flatter or slightly positive metallicity profile whose slope does not change significantly with Z. The high-α sequence effectively ends at $R \gtrsim 10$ kpc (shown previously in Figure 8, meaning there are not enough high-α stars in the outer Galaxy to constrain the metallicity profile past $R \gtrsim 10$ kpc.

The total disk looks like the high-α profile near the center of the Galaxy, and matches the low-α profile in the outer Galaxy. This is due to the relative weights between these two populations at different locations: as shown in Section 3.2, the inner region of the Galaxy is dominated by the high-α sequence, and the outer region is mostly low-α stars.

For each median metallicity profile, we quantify the gradient by fitting a straight line to stars with Galactocentric radius $R \geq 7$ kpc, where the profile reasonably approximates a single line. The best-fit slope for each profile is shown in Figure 14 against height above the plane Z, and tabulated in Table 1. The total population and the low-α population have steep negative profiles in the outer Galaxy, which approach zero as it moves above the plane. The high-α slope is close to

zero everywhere. Note that if we change the definition of our measured gradient and instead fit without the radial limit of ($R \geq 7$ kpc), the high-α population show a slight positive gradient, consistent with other studies (e.g., Vickers et al. 2021).

These results are generally consistent with previous results from a variety of methodologies. We measure a slope of -0.063 ± 0.001 dex kpc^{-1} for the total population close to the Galactic plane ($|Z| \leq 0.125$ kpc). Using previous data releases of APOGEE, Feuillet et al. (2019) measured the slope of the low-α metallicity gradient to be -0.059 ± 0.010 dex kpc^{-1}. Using open clusters as tracers, Donor et al. (2020) measured a radial gradient of -0.068 ± 0.001 dex kpc^{-1} with APOGEE DR16 data, and Myers et al. (2022) measured -0.073 ± 0.002 dex kpc^{-1} with DR17. Using Gaia DR3 data, Gaia Collaboration et al. (2022) measured a slope of -0.056 ± 0.007 dex kpc^{-1} for their bin closest to the Galactic plane. Additional studies use Cepheid stars as tracers and find similar results, with Genovali et al. (2014) reporting -0.060 ± 0.002 dex kpc^{-1}, and Lemasle et al. (2018) reporting -0.045 ± 0.007 dex kpc^{-1}. The large sample size, distance range, and high precision of the APOGEE DR17 sample enable us to map the radial, vertical, and α-dependence of the metallicity gradient in unprecedented detail. Differences between tracer populations used may explain the slight differences among previous results — e.g., Cepheids tend to be young stars that are more concentrated to the mid-plane, which alone results in a steeper vertical gradient.

These findings are also generally consistent with Hayden et al. (2014), who measured the metallicity gradients as a function of position (R and Z) in the disk and documented a relatively flat gradient near the center of the Galaxy, a steeper gradient further out in the disk, and generally flat gradients for the high-α population (Hayden et al. 2014, Table 2). Our data set is significantly larger than that of Hayden et al. (2014), with the inclusion of Southern Hemisphere observations, which leads to better spatial coverage in both the inner and outer regions of the Galaxy and less sensitivity to potential systematics. This may be why our radial gradient -0.063 ± 0.001 dex kpc^{-1} is slightly shallower than the -0.073 ± 0.003 dex kpc^{-1} from Hayden et al. (2014) for a comparable spatial zone.

Numerical simulations from Rahimi et al. (2014) reproduce similar gradient trends where the radial metallicity gradients flatten with increasing Z. Notably, they attribute the slight positive gradient of the Milky Way's thick disk to the flaring of younger populations at large radii. The vertical flaring of the disk has been documented extensively in other studies as well (e.g., Bovy

$|Z|$ (kpc)	Total	Low-α	High-α
0.0	-0.063 ± 0.001	-0.066 ± 0.001	-0.007 ± 0.005
0.25	-0.058 ± 0.001	-0.064 ± 0.001	-0.009 ± 0.004
0.5	-0.053 ± 0.001	-0.066 ± 0.001	-0.004 ± 0.003
0.75	-0.039 ± 0.002	-0.054 ± 0.002	0.006 ± 0.003
1.0	-0.023 ± 0.002	-0.044 ± 0.002	-0.002 ± 0.003
1.25	-0.013 ± 0.002	-0.028 ± 0.003	0.001 ± 0.004
1.5	-0.006 ± 0.002	-0.015 ± 0.003	0.004 ± 0.005
1.75	-0.001 ± 0.003	0.005 ± 0.005	-0.001 ± 0.005

Table 1. Radial metallicity gradients in dex kpc^{-1} as a function of height above the plane $|Z|$ from Figure 14.

et al. 2016; Mackereth et al. 2017; Lian et al. 2022a; Gaia Collaboration et al. 2022; Robin et al. 2022)

The models of Johnson et al. (2021), which incorporate radial and vertical redistribution of stars based on a hydrodynamical cosmological simulation of a Milky Way-like galaxy, also show a radial metallicity gradient that flattens with increasing $|Z|$.

The vertical median metallicity profile of the disk is shown in Figure 15, calculated in the same way as the radial gradients. The best slopes for all stars $|Z| < 2$ kpc are shown in Figure 16 and Table 2. Consistent with Gaia Collaboration et al. (2022), we find the gradients in the disk to be vertically symmetric. The slope measured above the disk ($Z > 0$) does not differ significantly from the slope measured below the disk ($Z < 0$). The total population has a steep negative vertical gradient close to the center of the Galaxy ($R < 5$ kpc), which flattens moving out in radius. This is generally true for the low-α population as well, although the innermost parts of the Galaxy ($R < 2$ kpc), show a very flat profile, possibly due to the bulge or bar. The high-α population has a shallow negative gradient everywhere, which does not significantly change with radius. Past $R \gtrsim 10$ kpc, the vertical gradient for the total, high-α and low-α populations are all close to zero.

This is also consistent with previous studies (e.g., Hayden et al. 2014, Table 1), where the vertical metallicity gradient approaches 0 as radius increases. Near the solar neighborhood, we report a vertical median metallicity gradient of -0.322 ± 0.009 dex kpc^{-1}. Hayden et al. (2014) report a gradient of -0.31 ± 0.01 dex kpc^{-1} in a comparable spatial zone. For the thick disk, Carrell et al. (2012) measured a vertical metallicity gradient of -0.113 ± 0.010, using stars close to the solar neighborhood with heights $1 \le |Z| \le 3$, consistent with our measurement of -0.115 ± 0.014 near the solar neighborhood for the high-α population.
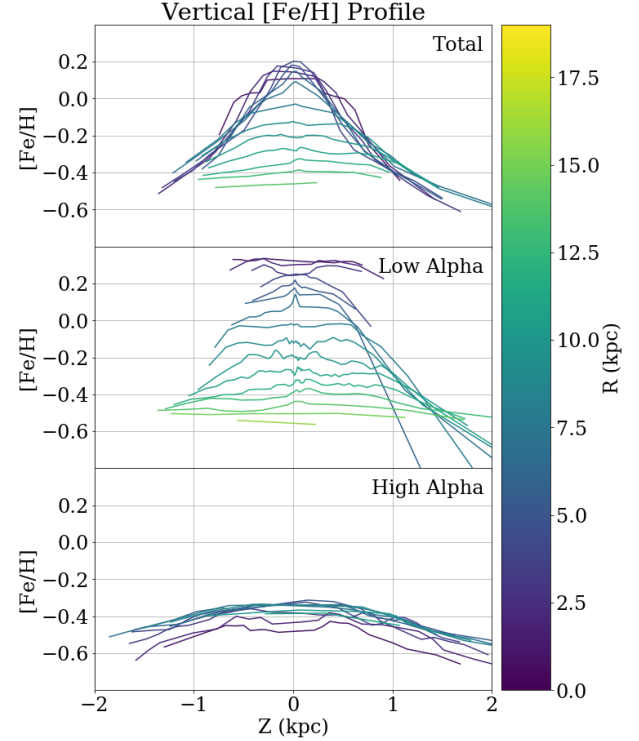
Figure 15. Vertical median metallicity profile as a function of Galactocentric radius (line color) for the total stellar population (top panel), the low-α disk (middle panel), and the high-α disk (bottom panel).
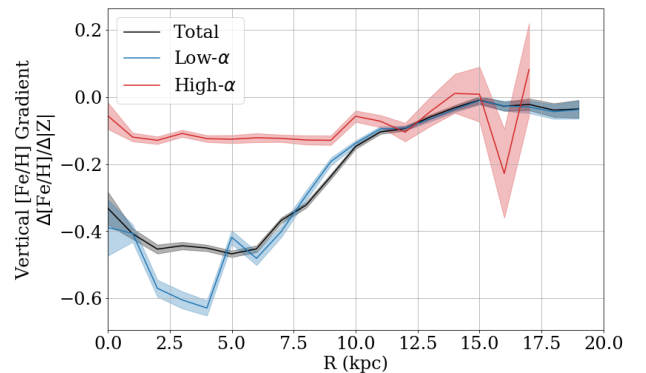
Figure 16. The best-fit slope for each vertical metallicity profile in Figure 15, fit with a single line for stars beyond $R > 7$ kpc for the total sample (black line), and the low-α (blue line) and high-α (red line) samples independently. The shaded region indicates the $\pm 1\sigma$ uncertainty in the slope measurement.

Examining the Galaxy's metallicity profile as a function of age provides a direct link to the evolution history of the disk. Figure 17 shows the radial (top panel) and vertical (bottom panel) metallicity profile for the low-α disk only, separated into bins of stellar age. In both cases, the slope of the profile flattens with increasing age.

R (kpc)	Total	Low-α	High-α
0.0	-0.331 ± 0.049	-0.126 ± 0.077	-0.055 ± 0.034
2.0	-0.453 ± 0.013	-0.501 ± 0.024	-0.103 ± 0.01
4.0	-0.45 ± 0.01	-0.558 ± 0.02	-0.089 ± 0.01
6.0	-0.453 ± 0.01	-0.421 ± 0.017	-0.083 ± 0.013
8.0	-0.322 ± 0.009	-0.278 ± 0.013	-0.115 ± 0.014
10.0	-0.148 ± 0.007	-0.132 ± 0.008	-0.051 ± 0.016
12.0	-0.094 ± 0.006	-0.087 ± 0.007	-0.08 ± 0.028
14.0	-0.032 ± 0.008	-0.033 ± 0.008	-0.0 ± 0.052
16.0	-0.027 ± 0.014	-0.024 ± 0.014	-0.02 ± 0.095
18.0	-0.039 ± 0.02	-0.039 ± 0.02	

Table 2. Vertical metallicity gradients in dex kpc^{-1} as a function of Galactocentric Radius R from Figure 16.

This is the opposite of what is predicted by the inside-out growth of the Galaxy (e.g., Matteucci & Francois 1989; Bird et al. 2013), where the gradient in the interstellar medium is expected to flatten out over time (e.g., Pilkington & Gibson 2012; Gibson et al. 2013; Mollá et al. 2018). The opposite trend, seen here, is commonly attributed to be a signature of radial migration (e.g., Wang & Zhao 2013; Magrini et al. 2016; Minchev et al. 2018; Vickers et al. 2021). However, an alternate explanation is also presented in Chiappini et al. (2001)textcolorred, where a disk formed from pre-enriched gas starts with an initially flat metallicity gradient that steepens over time.

3.5. *Metallicity Distribution Function*

While the radial and vertical median metallicity gradients in the disk reveal interesting general trends, more insights can be gleaned from the full metallicity distribution function (MDF) at different locations in the disk. Specifically, the spread and shape of the underlying MDF can be crucial for characterizing the complex history of the disk more accurately.

Figure 18 demonstrates how the metallicity distribution function varies with radius for samples at different vertical slices, from closest to the Galactic plane (right) to furthest above (left). Every third row is annotated with a white line and tick marks denoting the 25th, 50th (median), and 75th percentile of that row's distribution. The diamond point is the peak (or mode) of the distribution. Close to the plane (left panel), the characteristic metallicity (whether median or mode) decreases with radius. The shape of the MDF changes as a function of radius; close to the center of the Galaxy, the distribution is heavily skewed towards lower metallicities (the peak trends right of the median), and in the outer Galaxy the distribution is skewed towards higher metallicities (the peak is left of the median). This is consistent with the
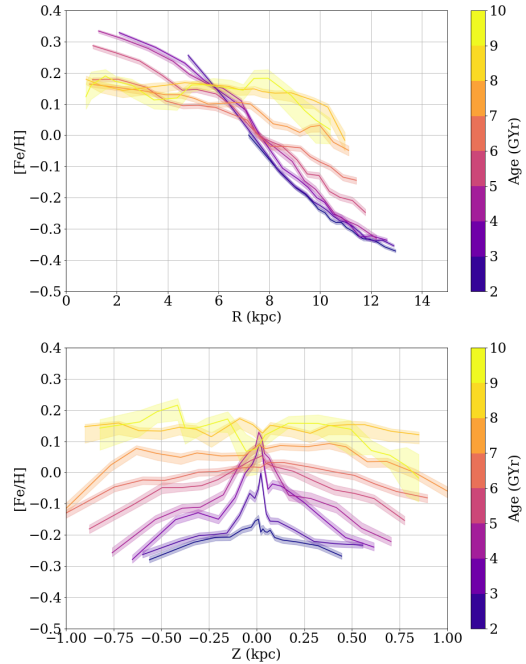

Figure 17. Top panel: the radial R median metallicity profile of the low-α disk, split into different samples of stellar age (line color). Bottom panel: the vertical (Z) median metallicity profile of the low-α disk, split into different samples of stellar age (line color).

trend seen in previous studies (e.g., Anders et al. 2014; Hayden et al. 2015; Loebman et al. 2016; Katz et al. 2021).

Figure 19 is the same as Figure 18, but further split into the low-α (blue) and high-α (red) disk samples to show how the MDF differs between the two. The white annotation lines are the same as in Figure 18, showing the distribution of the full sample for comparison. In the inner Galaxy, there is little overlap between the low-α and high-α MDF. In fact, the high-α population alone is what creates the metal-poor tail of the total MDF in Figure 18. Just outside the solar neighborhood ($8 < R < 12$ kpc), the MDF of the high-α and low-α populations overlap chemically. Moving above the plane, this overlap starts closer to the center of the Galaxy, around $R = 5$ kpc at $|Z| > 1.0$ kpc.

The high-α MDF is consistently broader than the low-α, has a shallower characteristic gradient, and shows less of a skewness trend with radius; the peaks (diamond points) are closer to the median (center tick mark) in general. Stars in the low-α sample transition from be-
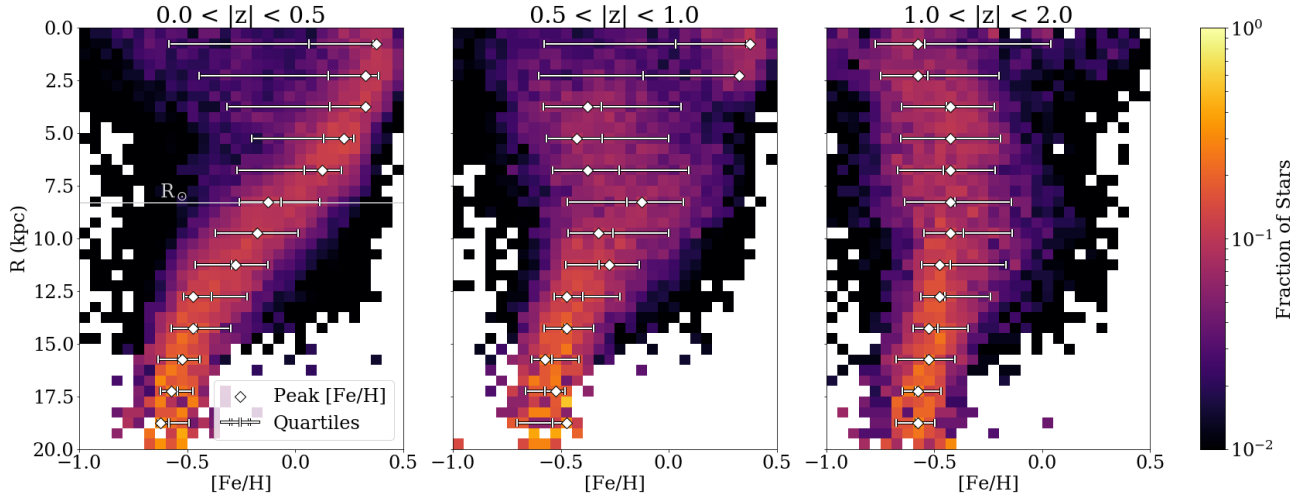
Figure 18. The metallicity distribution function of the Milky Way disk, split into different height bins (panels), from closest to the Galactic plane (left) to farthest above (right). Each panel shows the fraction of stars at each metallicity [Fe/H] as a function of Galactocentric radius. Every third row is annotated with markings for the peak (or mode) of the distribution (white diamond), as well as the 25th, 50th (median), and 75th percentiles (white tick marks) to highlight the shape of the distribution.
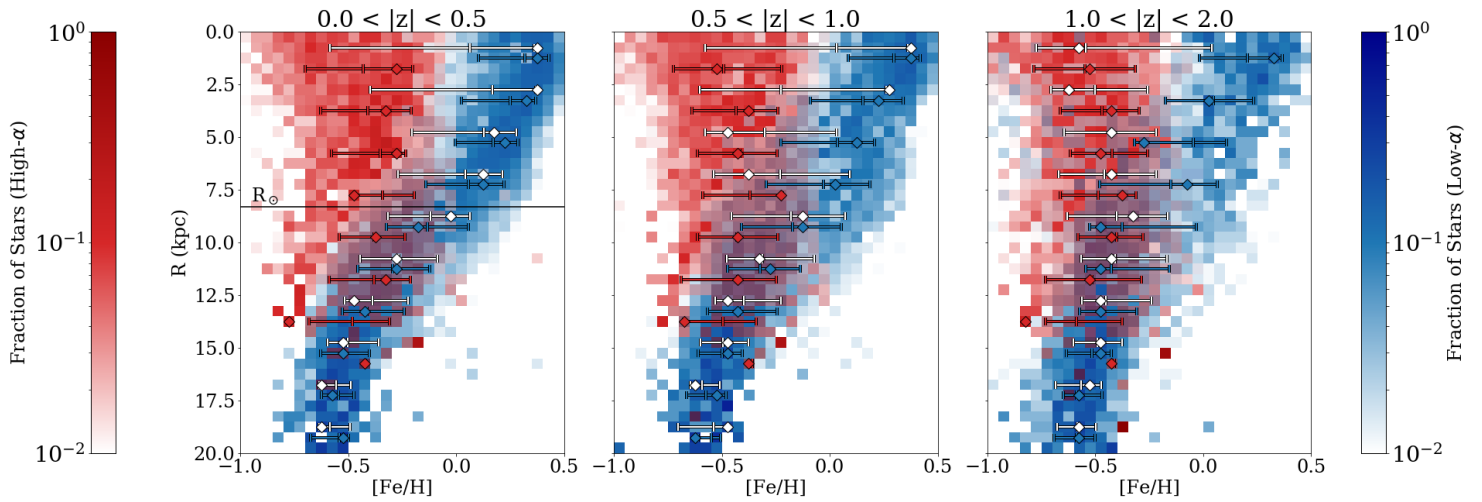

Figure 19. Same as Figure 18, further split by color between high (red) and low (blue) alpha samples

ing negatively skewed in the inner Galaxy to positively skewed in the outer Galaxy (as shown in Figure 20). However, this trend is not seen as strongly in the high-α disk, even at similar Galactic heights as the thin disk. Because the high-α population is generally older, this could imply that the high-α sample is more "mixed" vertically, meaning the birth location of stars tend to be further away from their present-day location, largely because they have had more time to move around.

Hayden et al. (2015) show this trend and present a simplified model to show that radial migration could

explain the change of the MDF shape with radius, because more stars migrate outward from the inner disk than vice versa. Loebman et al. (2016) and Johnson et al. (2021) show that this explanation succeeds quantitatively in models with realistic radial migration from cosmological simulations. These studies also show that the MDF shape becomes less pronounced at high |Z|, in agreement with the results of Figure 18 and Hayden et al. (2015).

Some simple statistics can be measured to more fully characterize the MDF as a function of radius; shown
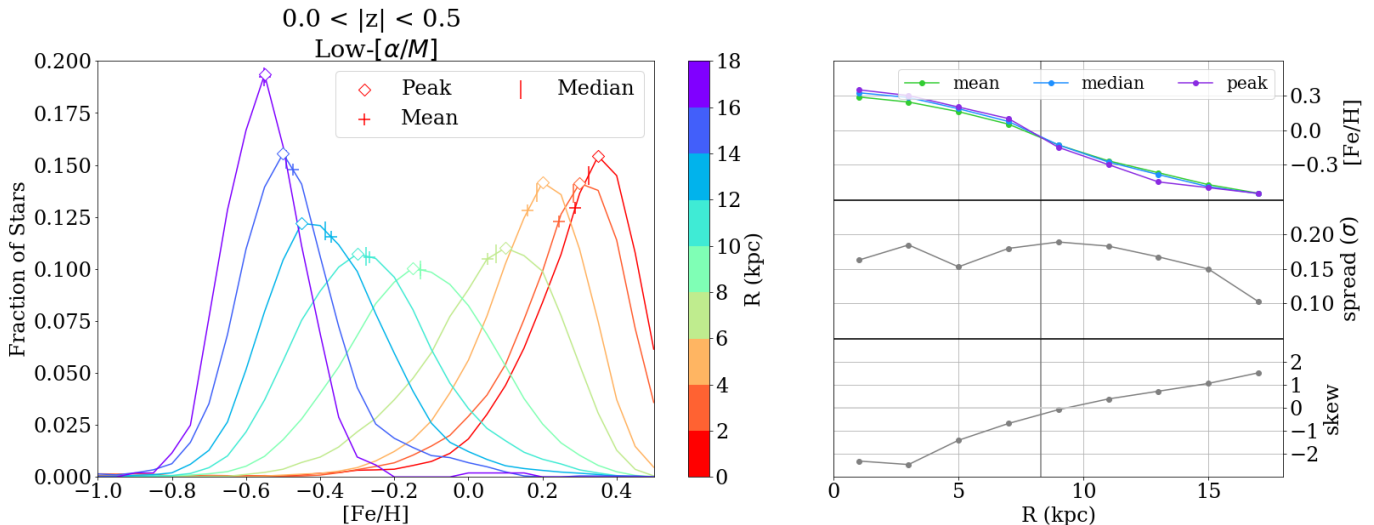
Figure 20. The metallicity distribution function (MDF) and its first three moments, limited to the low-α sample and close to the Galactic plane ($|Z| < 0.5$ kpc; equivalent to the left panel in Figure 18). **Left Panel:** The MDF at different radii in the Galaxy (colored lines). The right panels show the first three statistical moments for quantifying this distribution as a function of radius. **Top Right:** A characteristic [Fe/H] for each distribution function, measured as a median (blue line), a mean (green line) and the peak (or mode; purple line). **Middle Right:** The width, σ, of the distribution. **Bottom Right:** The skewness of the distribution, where a negative number indicates a left-leaning distribution as shown in the left panel and a positive number corresponds to a right-leaning distribution. The solar position ($R = 8.3$ kpc) is marked by a vertical gray line in all right panels.

in Figure 20 for the case of the low-α disk close to the Galactic plane (equivalent to the far left panel of Figure 18). The top right plot shows three definitions for a characteristic value for [Fe/H]; the mean, median, and peak of each distribution as a function of radius. While these values are similar, they are not identical, meaning the measured metallicity gradient of the disk will depend on the parameterization of [Fe/H] chosen. In the inner disk, the peak [Fe/H] is up to 0.1 dex higher in metallicity than the mean and median, due to the distributions being skewed metal-rich. In the outer disk, the peak is preferentially more metal-poor. Therefore, a metallicity gradient measured using the peak metallicity as a tracer will have a steeper slope than a gradient measured with the mean metallicity for the same group of stars.

The middle right panel in Figure 20 quantifies the spread of each distribution with radius, as total standard deviation σ. The outer regions of the disk ($R > 10$ kpc) are characterized by narrower distributions with less overall spread, whereas the inner disk MDFs span a larger range of metallicities.

The bottom right panel quantifies the skewness of each distribution with radius. The MDF in the inner regions of the disk it is negatively skewed, and in the outer regions it is positively skewed, quantifying the trend seen earlier Figure 18.

3.6. *Age Gradients*

The present-day distribution of stellar ages can act as an interesting snapshot as to what the Milky Way might have looked like at different points in time, while also documenting how stars might move and migrate away from their radius of birth.

The radial median age profile of the Milky Way is presented in Figure 21, identical to the way the metallicity gradients in Section 3.4 were calculated. The best-fit slope for each profile is shown in Figure 22, once again calculated only using stars with $R \geq 7$ kpc where the profile reasonably approximates a straight line.

The high-α population is generally flat everywhere, with a slope close to 0 at any height above the plane. The total and low-α stellar populations have a negative radial median age gradient in the outer Galaxy, while in the inner Galaxy the profile flattens out. The measured slope is flattest close to the disk ($z = 0$), and becomes negative moving above the plane. The total and low-α stellar populations have a vertical gradient that varies with radius as well. The vertical gradient is steeper closer to the center of the Galaxy, and flatter at large radii, similar to the vertical metallicity gradient.

3.7. *Age Distribution Function*

As before with metallicities, more information lies in the shape of the age distribution function at different locations in the Galaxy rather than the gradient alone. Figure 23 depicts the age distribution function (ADF) as a function of Galactocentric radius for different heights
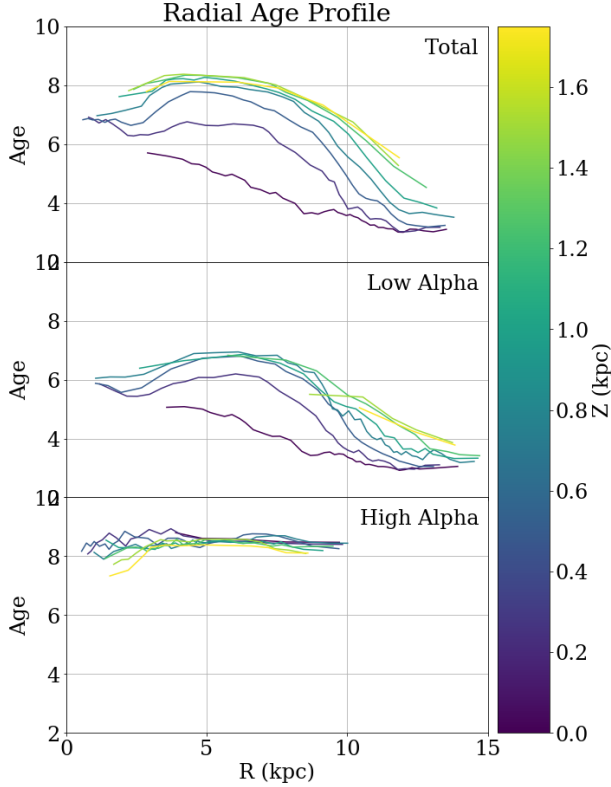
Figure 21. Radial median age profile as a function of height above the plane (line color), for the total stellar population (top panel), the low-α disk (middle panel), and the high-α disk (bottom panel).
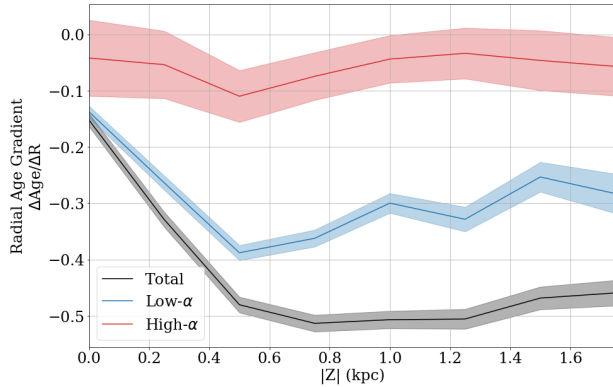
Figure 22. The best-fit slope for each radial age profile in Figure 21 in units of Gyr kpc^{-1}, fit with a single line for stars beyond $R > 7$ kpc for the total sample (black line), and the low-α (blue line) and high-α (red line) samples independently. The shaded region indicates the $\pm 1\sigma$ uncertainty in the slope measurement.

in the disk. Close to the Galactic plane (left panel), the peak age gradually declines, peaking around 7.5 Gyr near the Galactic center and 3 Gyr near the and outward. The spread of the ADF is fairly broad, spanning

up to 5 Gyr at all radii. In the outer Galaxy, the ADF is preferentially skewed toward older ages. Katz et al. (2021) found the ADF skewed towards younger ages in the inner Galaxy, and skewed towards older ages in the outer Galaxy, but they limited their investigation to just the low-α, thin disk sample.

Farther above the Galactic plane (middle and right panels of Fig. 23), the profile does not show a single gradient, but rather has a slight positive age gradient until $R \sim 5$ kpc which transitions into a negative gradient at larger R. After $R \sim 12$ kpc, the gradient flattens out. We caution that this flattening of the gradient at large R may be artificially induced by the lack of [Fe/H]< -0.5 dex stars in our sample when dealing with ages imposed by the sample cuts described in Section 2.4.

Figure 24 shows the age distribution function in the same way, but separated further into the low-α and high-α samples. Close to the Galactic plane (left panel), and in the inner Galaxy, there is some minimal overlap between the low-α and high-α samples, but near the solar neighborhood and outward, the ADF is more bimodal and there is more separation between the high-α and low-α ADF. At all radii, the low-α sample has a narrower distribution, and transitions from being skewed toward younger ages in the inner Galaxy to being skewed toward older ages in the outer Galaxy. This is similar behavior to the MDF in Figure 19, and also seen by Katz et al. (2021). Farther above the plane, there is more overlap between the low-α and high-α samples in the inner Galaxy, but there is still little overlap at larger radii.

Despite the similarities in these representations of the ADF to the corresponding ones for MDFs, we caution that the age uncertainties (typically ~ 0.1 dex) are significant relative to the total spread, which is not the case for the [Fe/H] measurements.

3.8. Age-Metallicity Relation

The relation between stellar age and metallicity has long been sought after to help constrain chemical evolution models (e.g., Twarog 1980; Edvardsson et al. 1993). In a simple "closed box" system, the metallicity of stars should increase over time, as each generation of stars enriches the interstellar gas from which subsequent generations are born. The actual scenario is much more complex, depending heavily on gas inflow and outflow rates, supernovae yields, stellar migration, and the positionally variable star formation history of the Galaxy. Observations of the age-metallicity relation in the Milky Way include the effects of all of these processes, and they therefore provide a powerful constraint for chemical evo-
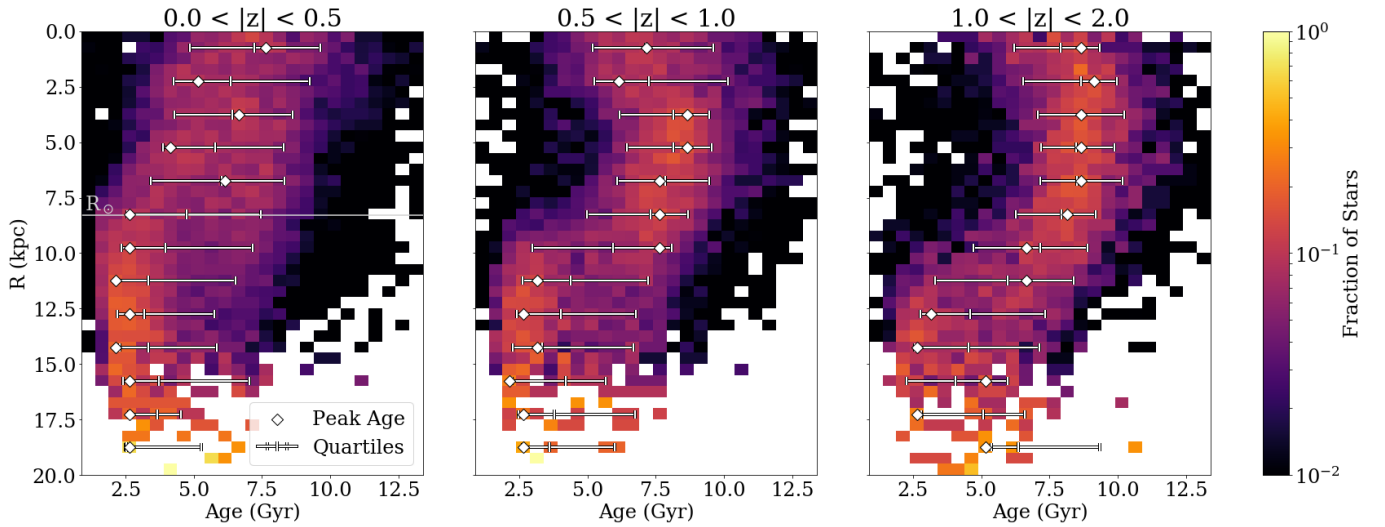
Figure 23. The age distribution function of the Milky Way disk, split into different height bins (panels), from closest to the Galactic plane (left) to farthest above (right). Each panel shows the fraction of stars at each age as a function of Galactocentric radius. Every third row is annotated with marks for the peak (or mode) of the distribution (white diamond), as well as the 25th, 50th (median), and 75th percentiles (white tick marks) to highlight the shape of the distribution.
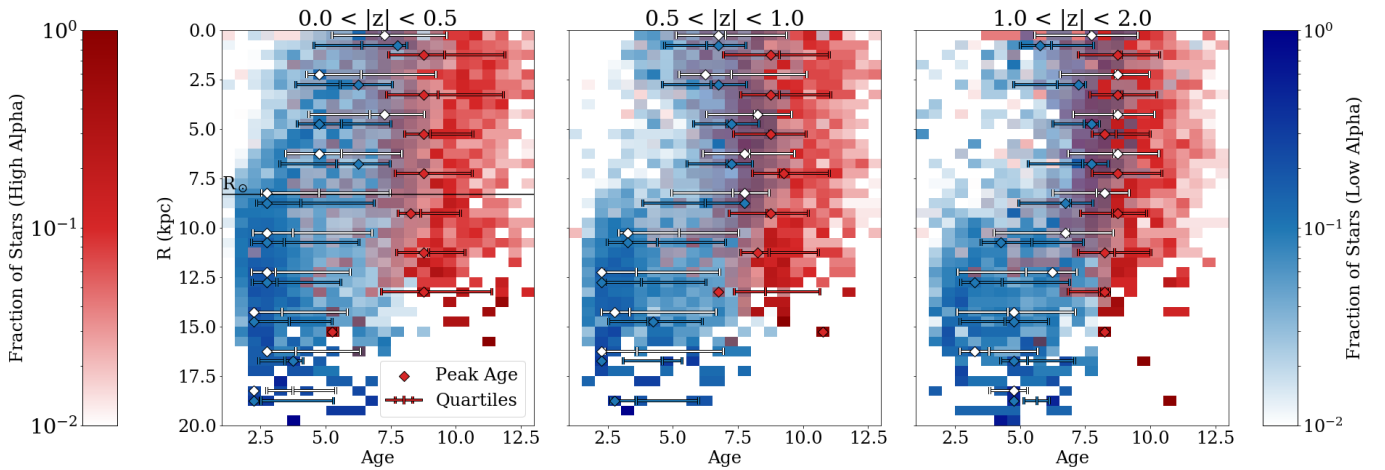

Figure 24. Same as Figure 23 but further split by low- (blue) and high-α (red).

lution models to reproduce across different locations in the Galaxy.

Previous studies have found significant scatter in the age-metallicity relation (AMR) near the solar neighborhood, where stars with a single age span a wide range of metallicities, which cannot be attributed to observational errors alone (e.g., Casagrande et al. 2011; Bergemann et al. 2014; Aguirre et al. 2018; Lin et al. 2018; Grieves et al. 2018; Sahlholdt et al. 2022; Xiang & Rix 2022). The AMR also varies with Galactic location, making it difficult to constrain a single relation that fits the whole disk (e.g., Hasselquist et al. 2019; Feuillet et al. 2019; Casamiquela et al. 2021; Lian et al. 2022b).

The AMR for our sample of stars in the Milky Way disk is shown in Figure 25. The data are split into bins

of radius (columns), and height (rows), to demonstrate how the age-metallicity relation varies across Galactic location. Points are colored by α-element abundances, which are known to be more tightly correlated with age, although the exact trend depends on Galactic position (e.g., Haywood et al. 2013; Nissen 2015; Bedell et al. 2018; Feuillet et al. 2018; Hasselquist et al. 2019; Lian et al. 2022b, see also Section 3.9). The median trend across different bins in age is tracked as black square points to help guide the eye. Note that the x-axis (stellar age) has been reversed so that older stars are on the left, better expressing the forward flow of time. The x-axis is also presented in log space, which is more representative of the uncertainties in our age estimates (Section 2.4).
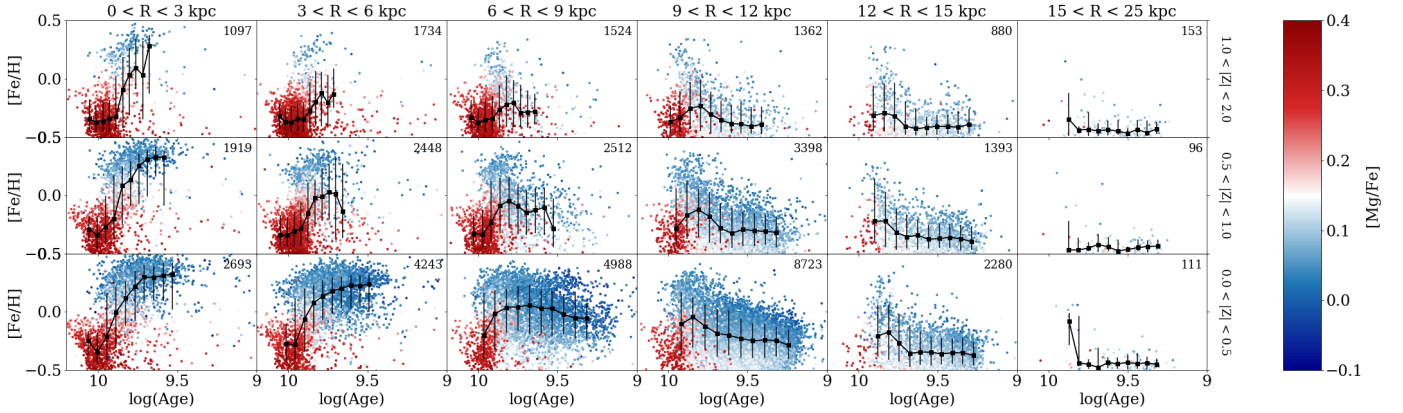
Figure 25. The age-metallicity relation across the Milky Way disk. Panels represent different spatial zones, laid out in the same way as Figure 8, with rows corresponding to Z and columns increasing in R. The number in the top-right corner of each panel is the number of stars in our sample in that spatial bin. The age and metallicity for individual stars is plotted, colored by [Mg/Fe] abundance. The running median trend is plotted in black square points to guide the eye, with the vertical bars indicating the standard deviation in [Fe/H] for bins in log(age).

One can also read each panel rotated 90° to see the distribution of log(age) at fixed [Fe/H].

Consistent with previous studies, there is significant scatter around the age-metallicity relation near the solar neighborhood. There is a slight gradient in α-element abundances within that spread; nearly everywhere in the Galaxy, higher-metallicity stars are relatively more alpha-poor.

The age-metallicity relation has less scatter moving towards the inner Galaxy (left column), and above the plane (top row). This implies that the in-situ age-metallicity relation of the inner galaxy has been more preserved, and less contaminated by migrated stars; or in other words, more stars migrate outwards than inwards in the Galaxy. This is perhaps not surprising; dynamically, stars in the inner Galaxy migrate outwards, and stars in the outer Galaxy migrate inwards (e.g., Sellwood & Binney 2002). The inner Galaxy is denser than the outer disk, so if one assumes the same rate of migration across all radii, more stars would migrate outwards simply because more stars start in the inner Galaxy. The age-metallicity relation shown in Sahlholdt et al. (2022) also shows a lower dispersion for the inner regions of the disk (their "Pop C" sample) using GALAH data.

The AMR is steepest in the inner Galaxy, and flattens moving out in radius. In all panels, the age-metallicity relation flattens out at young stellar ages, having perhaps reached chemical equilibrium where inflowing gas dilutes the ISM at the same rate as it is being enriched (e.g., Dalcanton 2007; Finlator & Davé 2008; Weinberg et al. 2017). In the inner disk, the equilibrium metallicity is higher than the equilibrium metallicity reached in the outer disk and moving beyond the mid plane.

Equilibrium seems to have been reached sooner (at older stellar age) in the outer disk than the inner disk.

There is a notable inversion of the AMR at large radii in the Galaxy, where older stars trend more metal-rich than the younger stars in the sample. This is also reported in Hasselquist et al. (2019) and Lian et al. (2022b). The cosmological simulations of Lu et al. (2022) explore the possible origins of such an inversion, suggesting that it could be the signature of interactions with a satellite galaxy like the Sagittarius dwarf, and radial migration notably widens the apex.

A recent study from Xiang & Rix (2022) documented a disjointed age-metallicity relation for the sum of the total disk, suggesting the two-infall scenario or a major merger is responsible. In our results, we see some evidence of bimodality in Figure 26, which is a contour map of the point density distribution in Figure 25. In the inner Galaxy ($R < 3$ kpc), the age-metallicity relation has two separate peaks.

3.9. Age-Alpha Relation and Chemical Clocks

While no clear correlation between age and metallicity relation exists near the solar neighborhood, better correlation has historically been found between age and α-element abundances (e.g., da Silva et al. 2012; Haywood et al. 2013; Bensby et al. 2014), leading some to use α-elements as a chemical clock, substituting their abundances when stellar ages are not readily available. Even so, the [Mg/Fe]-age correlation has been found to vary across the Milky Way's disk (e.g., Aguirre et al. 2018; Feuillet et al. 2018; Vázquez et al. 2022), extending the metaphor to imply that chemical clocks run in chemical "time zones". Reproducing this variation has
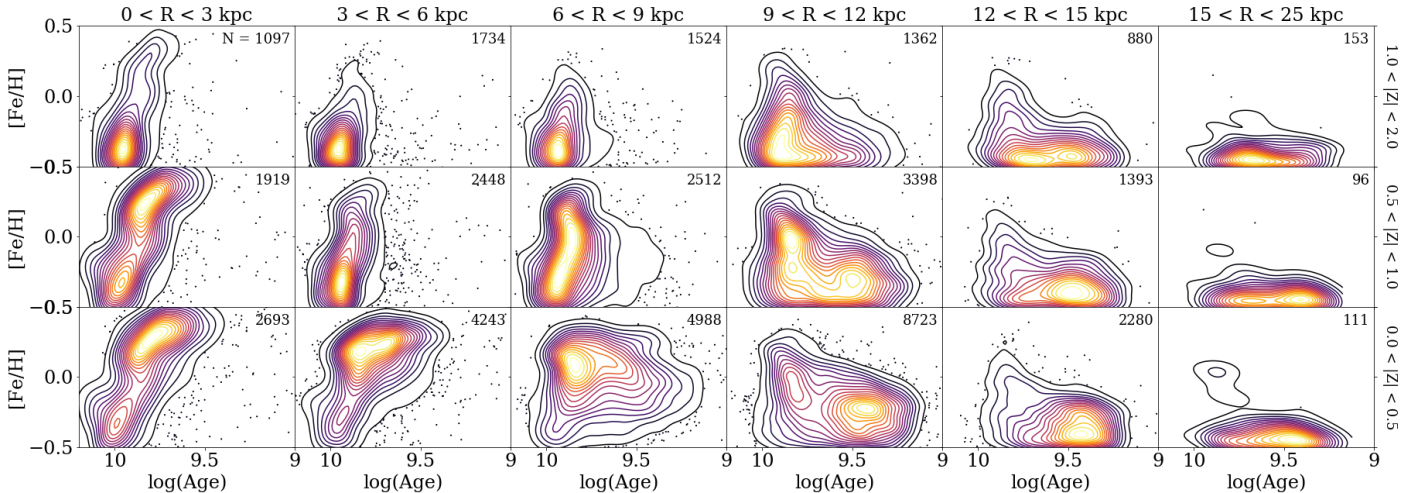
Figure 26. Same as Figure 25, but showing the contours of point density in each panel.

been considered a strong constraint on chemical evolution models (e.g., Haywood et al. 2013; Spitoni et al. 2019a; Johnson et al. 2021).

In Figure 27, we show the relation between age and [Mg/Fe] as a contour plot at various locations throughout the disk. The distribution is double-peaked in nearly all panels, with the older, low-α population most prevalent above the disk and in the inner Galaxy. Near the solar neighborhood and outward, the relation of the low-α sequence is relatively flat, with a large spread in ages corresponding to a small range of [Mg/Fe] abundances. This is consistent with the findings of Haywood et al. (2013) and Feuillet et al. (2018). In the inner Galaxy, a small range in [Mg/Fe] abundances corresponds more tightly with a smaller range in age, a phenomenon that applies, though differently, to each the high-α and low-α groups. As in Haywood et al. (2013), there is some age overlap between the two sequences, implying that the low-α sequence in the outer disk began forming stars while the high-α disk was concurrently still forming stars in the center of the Galaxy.

For the low-α sequence, there is some evolution with Galactic position. The low-α stars are older and more alpha-poor near the center of the Galaxy. In the outer Galaxy, the sequence is more α-enhanced and generally younger, although covering a larger spread in ages. Above the plane ($Z > 1$ kpc), the low-α sequence is more α-enhanced.

The high-α sequence stays generally in the same location on this diagram regardless of position in the Galaxy. This is similar to the trend seen in Figure 8 and 10, where the locus of the low-α sequence changes signifi-

cantly with Galactic position while the high-α sequence stays largely in the same location.

In the $R = 9 - 12$ kpc and low-$|Z|$ zones, the log(age) distribution is bimodal even within the low-α sequence. This could be evidence for a three-phase star formation history. Sahlholdt et al. (2022) report a similar distribution in the age-metallicity relation of their "Pop A" sample, which probes a similar location in the disk. The younger peak in log(age) appears similar to the recent starburst 2-3 Gyr ago detected independently in Isern (2019) and Mor et al. (2019).

3.10. Chemical Evolution via Chemical Tagging

If a group of stars was born together in the same location and at the same time, they should have identical chemical abundances ([Fe/H] and [Mg/Fe] in our case). This is the basic assumption behind "chemical tagging", used to identify stellar siblings that have been redistributed throughout the Galaxy despite being born together (e.g., Hawkins et al. 2015; Ting et al. 2015; Price-Jones et al. 2020; Buder et al. 2021). We can turn this assumption around and use the fact that if a group of stars has the same age and chemical abundances, they were likely born in a small spatial region in the Galaxy. Using this, we can track the spatial redistribution of the population over time, as well as look at the enrichment history of an area of the Galaxy for fixed metallicity.

Figure 28 shows this evolution for stars close to solar metallicity ($-0.1 \leq$ [Fe/H] ≤ 0.1 dex). The present-day radial distribution (x-axis) and [Mg/Fe] abundance (y-axis) is shown for different bins in stellar age (line color) for both the low-α (solid lines) and high-α populations as the contour containing 75% of all points in that bin. Stars at the same age and metallicity should all have
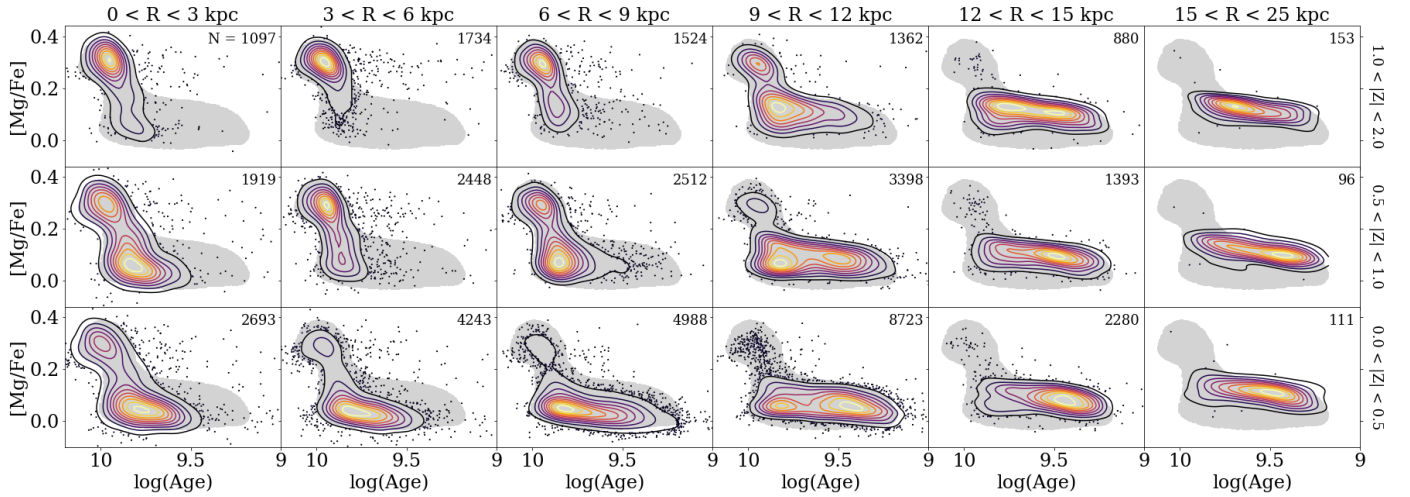
Figure 27. The age-alpha relation across the Milky Way disk. Panels represent different spatial zones, laid out in the same way as Figure 8. The contours represent the density of points on the diagram. The gray background shape outlines the 90% contour for the entire sample, and is the same in all panels for reference.
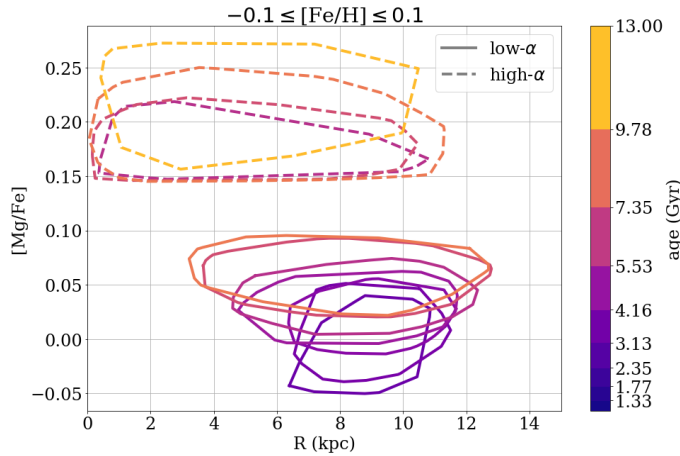
Figure 28. The radial distribution of the low-α (solid lines) and high-α (dashed lines) populations shown as the contour containing 75% of all points for different bins in stellar age (line color) all at fixed $-0.1 \leq$ [Fe/H] ≤ 0.1.

same [Mg/Fe] abundance. If stars did not move from where they were born, we would expect to see a tight clump in this space. If stars migrate significantly over time, the shape of the clump should spread out with stellar age, but keep the same [Mg/Fe] abundances (or a "flat slope" in [Mg/Fe]). If the slopes were not flat, it may be indicative of different enrichment histories for different parts of the Galaxy; suggesting a violation of the assumption that stars with the same metallicity and age were born roughly in the same place.

The young, α-poor stars in Figure 28 currently reside in a relatively confined clump in radius and [Mg/Fe] as expected. As stellar age increases, the shape of the

clump widens to cover a broader range in radius while the [Mg/Fe] abundnace remains confined. The high-α sequence does not show this evolution in width with time, but notably does not include enough young stars to properly trace this. As shown in Figure 9, high-α stars tend to be old.

As stellar age decreases, the [Mg/Fe] value covered by a population decreases for both the low-α (solid lines) and high-α (dashed lines) populations. This tracks the chemical evolution of a location in the Galaxy, as Type Ia supernovae begin "diluting" the interstellar medium with iron, thereby decreasing the overall [Mg/Fe] ratio.

4. DISCUSSION

Using large samples of stars to map the Milky Way in different parameter spaces using metallicity, α-element abundances, and age, as demonstrated here, has the potential to place strong constraints on chemical evolution models and reveal the major processes which formed our Galaxy. Directly comparing our results with specific chemical evolution tracks is beyond the scope of this paper, but in this section we qualitatively compare our results with predictions from the leading classes of chemical evolution models discussed in the Introduction; the 'two-infall', 'superposition', and 'clumpy formation' scenarios.

The underlying assumption necessary to interpret these results is that in a well-mixed interstellar medium, stars formed at the same time and the same place in the Galaxy will have the same chemical abundances (both metallicity and α-elements). Under this assumption, a spread in abundance at present day for stars at a given

age at the same location, whether bimodal or not, can only be produced if stars have moved away from their birth location.

4.1. *Superposition and Radial Migration*

The "superposition" class of evolution models (e.g., Schönrich & Binney 2009a,b; Minchev et al. 2013, 2014; Minchev et al. 2017; Johnson et al. 2021) explain the observed chemical bimodality in solar vicinity as the superposition of evolutionary tracks for stars born at different Galactocentric radii, with the stars having reached their present-day location in the solar neighborhood through radial migration. Several predictions made by these superposition chemical evolution models are seen in our results.

The metallicity gradient flattening with age (Figure 17) is predicted by radial migration (e.g., Sellwood & Binney 2002; Roškar et al. 2008; Wang & Zhao 2013; Hayden et al. 2015; Mackereth et al. 2017; Frankel et al. 2018, 2020; Vickers et al. 2021; Lian et al. 2022b). If stars are formed *in-situ* with a steep metallicity gradient, that gradient will flatten over time as metal-rich inner Galaxy stars migrate outwards and metal-poor outer Galaxy stars migrate inwards, skewing the metallicity distribution at either end of the Galaxy. The older stars in our sample show a flatter gradient than the younger stars; in agreement with this scenario.

The shape of the metallicity distribution function at different locations in the Galaxy (Figures 18 and 20), specifically the skewness or asymmetry of the MDF, can be a sign of radial migration if a population of stars has a metal-rich tail (e.g., Hayden et al. 2015; Loebman et al. 2016). Our data show a skewed MDF in Figure 20, where the inner region of the disk is negatively skewed, and the outer region of the disk is positively skewed. This trend is commonly attributed to radial migration, whereby migrating stars become the metal-rich tails in the MDF at different locations (e.g., Schönrich & Binney 2009a,b; Roškar et al. 2008; Hayden et al. 2015; Loebman et al. 2016; Johnson et al. 2021). The metal-poor tail in the inner Galaxy's MDF is likely attributed to a spread in ages between the stars, as is predicted by even closed-box chemical evolution tracks when any given location in the Galaxy becomes enriched over time (e.g., Romano & Starkenburg 2013; Vincenzo et al. 2014; Weinberg et al. 2017; Toyouchi & Chiba 2018). The metal-rich tail of the outer Galaxy's MDF is more difficult to explain with a traditional chemical enrichment track, which leaves radial migration as the most likely culprit.

The inversion in skewness in the MDF occurs around $R = 9.4$ kpc in our data. This could be linked to the Outer Lindblad Resonance (OLR) of the Milky Way disk; a resonance with the Galactic bar driving different dynamical effects throughout the disk, one of which is radial migration (Halle et al. 2015; Michtchenko et al. 2016; Dias et al. 2019; Khoperskov et al. 2020b). Using Gaia data, Khoperskov et al. (2020a) estimates the OLR to be located at a Galactocentric radius of around 9 kpc. Khoperskov et al. (2020b) uses a high-resolution N-body simulation to investigate the relationship between the OLR and radial migration, and find that stars from the inner Galaxy migrating outwards become "trapped" in the OLR. When the rotation period of the bar slows down, those stars can escape and migrate further out. The trapping effect of the OLR could also explain the build-up of metal rich stars at $R \sim 9$ kpc in Figures 5 and 6.

We also see signs of radial migration in the age-metallicity relation shown in Figure 25. Around the solar neighborhood, there is significant scatter about the age-metallicity trend. If the interstellar medium is always well-mixed, the large spread in metallicity for stars of a given age must mean that some of these stars were not born at their present-day location. This is another consequence of radial migration predicted by the superposition class of models, which explain the spread by emphasizing the difference between the present-day locations of stars and their birth radii (e.g., Schönrich & Binney 2009a; Wang & Zhao 2013; Minchev et al. 2013; Lian et al. 2022b). While any location in the Galaxy should start with a tight age-metallicity relation, migration will blur the present-day relation as metal-rich stars from the inner disk move outward and contaminate the more metal-poor outer disk. Radial migration is most efficient in the plane of the disk, therefore these models predict less spread in the age-metallicity relation at larger vertical heights, an effect also seen in our data.

The turnover in the age-metallicity relation, seen in Figure 25 and in Hasselquist et al. (2019), can also be explained through radial migration. The older, metal-rich stars were likely formed in the inner Galaxy, and migrated outwards to where they are found today, contaminating the age-metallicity relation. An alternate explanation could be the dilution of the ISM from pristine gas infall, lowering the metallicity of a previously-enriched area of the Galaxy (e.g., Spitoni et al. 2019a; Lu et al. 2022). However, in this scenario, it is predicted that both the high-α and low-α tracks in metallicity would still decrease with stellar age, with the post-dilution low-α track beginning at a lower-metallicity than the high-α track at the same time (e.g., Spitoni et al. 2019a). That predicted trend is not obvious in our data, and the large spread in metallicity at a given age favors a radial mi-

gration explanation. Lu et al. (2022) further explore the origin of such a turnover using cosmological simulations, and find that even when the turnover in the age-metallicity relation can be directly linked to the infall of a satellite galaxy, radial migration can widen the shape of the peak.

Vertical motions should also be considered. In the age-α relation of Figure 27, a population of stars with the same age and in the same present-day location can have a large spread in [Mg/Fe], most dramatically seen in the inner Galaxy ($R < 3$ kpc). This violates the underlying assumption mentioned earlier, meaning stars must have moved around to create that spread. However, in this case, *radial* migration is an unsatisfactory explanation, as stars from the outer Galaxy migrating inward is expected to be a less frequent occurrence than the other way around, simply a consequence from the density profile of the Galaxy (e.g., Sellwood & Binney 2002). Instead, the *vertical* motion of stars could result in the observed spread if stars born above the mid plane are currently found near $Z = 0$. Even stars formed above the plane will inevitably have vertical motions that cause their orbits to cross the plane, meaning this could be a natural consequence of a star's vertical orbit. Related vertical motions could be linked with dynamical heating (e.g., Spitzer & Schwarzschild 1951; Barbanis & Woltjer 1967; Lacey 1984; Mackereth et al. 2019) or the "upside-down" formation of the disk (e.g., Toth & Ostriker 1992; Quinn et al. 1993; Hänninen & Flynn 2002; Brook et al. 2004; Freudenburg et al. 2017; Bird et al. 2013, 2021). Using a quantity like guiding radius ($R_{\rm guide}$) and maximum height $|Z_{\rm max}|$ calculated from parameterized stellar orbits, instead of the present-day R and $|Z|$ we use here, may remove contamination by thick disk stars currently "passing through" the thin disk from these figures. Some studies, including Boeche et al. (2013), Katz et al. (2021), and Spitoni et al. (2022a), have looked at these quantities, and found similar overall trends.

The evolution of radial distribution with stellar age seen in Figure 28 is yet more evidence for radial migration. The youngest, low-α stars indicate that for a population of fixed age, [Fe/H], and [Mg/Fe], they are expected to be born at a similar radius in the Galaxy. As stellar age increases, the population redistributes into a larger range of R, showing that stars migrate radially over time. The high-α stars, which cover a similar range in Galactic radius despite a wide window in age ($5 \le$ age ≤ 13 Gyr), may suggest an "upper limit" on the efficiency of radial migration and the timescales over which stars can migrate on average; see e.g., Frankel et al. (2020) and Lian et al. (2022b) for such an analysis. Similarly, the relative distribution of stars within

the low-α contours may hint at the importance of direction in radial migration (i.e., what fraction of stars migrate outwards instead of inwards), although such a discussion is beyond the scope of this work.

This wide variety of results suggests that significant stellar migration occurs in the Milky Way disk, most affecting the trends seen close to the Galactic plane and at larger radii. However, there are open questions remaining about the nature of the inner disk, where an apparent bimodality exists that is not easily explained by migration models.

4.2. *Two-Infall or Major Merger*

The "two-infall" class of evolution models (e.g., Chiappini et al. 1997; Chiappini et al. 2001; Lian et al. 2020a,b,c; Spitoni et al. 2019a, 2020, 2021, 2022a) suggest that the two sequences in [Mg/Fe]-[Fe/H] space formed sequentially in time. Under this scenario, the thick disk was formed first during the initial collapse of the Galaxy, and after some time delay a second infall of gas fed the creation of the thin disk. These models predict several of the observed trends in our results, most notably in areas where radial migration is not as efficient, including the inner Galaxy and at greater heights above the Galactic plane.

In Figure 8, we show that the α-bimodality persists throughout the majority of the disk. This is significant because while the "superposition" class of chemical evolution models can produce the low-α "sequence" and broad distribution of [Mg/Fe] in the solar neighborhood using only radial migration (e.g., Schönrich & Binney 2009a,b; Minchev et al. 2013, 2014; Nidever et al. 2014; Sharma et al. 2021a; Johnson et al. 2021), radial migration is known to be most efficient close to the Galactic plane and in the outer disk. Therefore, the bimodality in other parts of the Galaxy is more difficult to explain with radial migration alone. Previous studies by Freudenburg et al. (2017) and Zasowski et al. (2019) report that the shape of the MDF and the [Mg/Fe]-[Fe/H] trends seen in the inner disk ($3 < R < 5$ kpc) could be modeled well using a single evolutionary track in an "upside-down" disk formation model. Here, however, we show that with more data, two distinct tracks of [Mg/Fe] are observed even in the inner Galaxy. This is also reported in Queiroz et al. (2021).

Near the solar neighborhood, radial migration models predict bimodality by explaining the high-α sequence as contaminants from the inner Galaxy; due to the intrinsic density profile of the Galaxy, more stars are expected to migrate outwards than inwards, so the inner Galaxy should display less contamination from the low-α sequence. This is in contradiction with our findings,

where the α-bimodality persists throughout the majority of the disk. Johnson et al. (2021) also report that the bimodality reproduced by their superposition model is weaker than the observed bimodality in the Milky Way; in particular, the model overproduces intermediate-α stars compared to observations. Chen et al. (2022) find greater success in producing bimodality with radial migration. However, a two-infall (or multi-infall) model may be needed to explain the bimodality in the inner Galaxy.

The age-metallicity relation in Figure 25 produces some trends that are better explained by the two-infall model than by radial migration. Minchev et al. (2013, 2014) report that while the scatter around the age-metallicity relation can be attributed to radial migration, the overall slope is only weakly affected. In our data, consistent with other recent studies (Feuillet et al. 2019; Hasselquist et al. 2019), the slope of the age-metallicity relation varies significantly with Galactic radius. This is reproduced with a two-infall model, where the low-α, post-infall disk has a shallower slope in the age-metallicity relation compared to the high-α population, due to the continuous inflow of gas diluting the disk that was not present during the formation of the original high-α disk (Spitoni et al. 2019a, 2020, 2021).

The apparent disk bimodality is not only observed in [Mg/Fe]-[Fe/H] chemistry, but also in the age-metallicity relation. Recent work by Xiang & Rix (2022) show a disjointed age-metallicity relation for the sum of the total disk, which is only possible to reproduce in a two-infall scenario or with a major merger event. In our study, the age-metallicity relation as a function of Galactic position (Fig. 25) also shows a possible bimodality, most apparent in the $0 < R < 3$ kpc range of the inner disk.

The age-α relation in Figure 27 is perhaps more of a "smoking gun", with clear bimodality in the relation persisting across nearly the entire disk. In the outer disk $(9 < R < 15)$, there appears to be an additional bimodality within low-α sequence, suggesting a three-phase star history similar to that detected in Sahlholdt et al. (2022) using a sample of stars from the GALAH survey. The uncertainties in our age estimates are not negligible, but are likely not responsible for this bimodality. Presumably, larger data uncertainties would blur out the distribution and decrease the observed bimodality. In fact, due to the age uncertainties, the "true" age bimodality in the Milky Way may be stronger than what is shown in our analysis. The peak of our "third" starburst is around 2-3 Gyr, consistent with the recent burst Isern (2019) and Mor et al. (2019) report, possibly linked to the most recent interaction with the Sagittarius dwarf spheroidal galaxy as

it passed through the disk (e.g., Ruiz-Lara et al. 2020; Laporte et al. 2019; Antoja et al. 2020)

In the age-alpha relation, the age overlap between the high-α and low-α sequences are impossible to explain with a single evolutionary track. In this interpretation, we do caution that if the transition from high-α to low-α is fast, uncertainties in age determination could produce an artificial impression of age overlap. Haywood et al. (2013) also detects an overlap in age, claim that the dichotomy in the solar neighborhood can be reproduced by the two-infall scenario, and that little to no radial migration is needed.

For the inner disk, the spread in [Mg/Fe] for a given age is likely due to the vertical motions of stars as discussed previously in Section 4.1. However, if the spread was purely from vertical blurring, a continuous spread would be observed, and not the bimodal distribution seen here.

In summary, the bimodality in [Mg/Fe] and stellar ages persisting across the inner disk is not easily explained through radial migration, which is most efficient at larger radii. A multi-phase star formation history, such as those presented in the two-infall model, better predicts the trends observed in the inner Galaxy.

4.3. Clumpy Star Formation Models

The "clumpy star formation" models (e.g., Clarke et al. 2019; Beraldo e Silva et al. 2020; Amarante et al. 2020) predict that the two sequences in α-element abundances formed simultaneously but in different modes: the high-α sequence formed in rapidly-enriched gaseous clumps and the low-α formed in a less efficient smooth disk.

One major result that the clump star formation models predict is the temporal overlap between the two α sequences: The low-α disk starts forming at the same time as the high-α sequence, meaning there should be some overlap in stellar ages between the two sequences. We see this overlap in Figure 25 and 27, where stars at around log(age) ~ 9.7 Gyr span a significant range in both metallicity and α-element abundances. This age overlap has also been observed in previous studies (e.g., Haywood et al. 2013; Hayden et al. 2017; Aguirre et al. 2018).

One potential avenue for further investigating the difference between the two-infall class of models and the clumpy star formation models lies not within the Milky Way but in other galaxies. If the two-infall model is true, a chemical bimodality would only be present in galaxies that experienced significant gas infall both at early and late times, meaning it would be a rare phenomenon only affecting approximately 5% of galaxies with comparable

mass to the Milky Way (e.g., Mackereth et al. 2018). In contrast, the clumpy star formation models predict that chemical bimodality would be more common in galaxies with comparable mass to the Milky Way, because star formation clumps are observed in more than 60% of high-redshift galaxies (e.g., Guo et al. 2015).

5. CONCLUSIONS

The large sample size, extensive spatial coverage, and precise abundance measurements for stars in the final data release of APOGEE can help provide strong constraints on Galactic formation and evolution models, in particular for its disk populations. We present results from the final data release of the combined SDSS APOGEE and APOGEE-2 surveys that explore the chemical and age structure of the Milky Way's disk, measure gradients and distribution functions, and link these new observational constraints to predictions from different chemical evolution models.

Our main conclusions are as follows:

- **Cartography:** Overall maps of the Milky Way disk show negative radial age and metallicity gradients. The bar/bulge stands out as more metal-rich and alpha-poor in the inner Galaxy compared to stars at similar radii but different azimuthal angles.

- **[Mg/Fe] Distribution:** The distribution of α-element abundances reveals the chemically bimodal disk structure in the Milky Way. The low-α disk is thinner (in Z) and more radially extended than the high-α disk. The locus of the low-α sequence varies with radius.

- **Azimuthal Variance of Metallicity:** We find no significant evidence of large-scale azimuthal asymmetry in most of the disk, although the Galactic bar stands out as metal-rich in the mid-height plane. In the solar neighborhood, we see some coherent, non-axisymmetric structure in metallicity, although it does not obviously correlate with the spiral arms.

- **Metallicity Gradients:** The Milky Way's full radial metallicity gradient is flat near the center of the Galaxy, and steepens further out in radius. The high-α disk displays a nearly flat metallicity profile everywhere in the Galaxy, and the low-α disk has a negative gradient that is shallower at high Z than it is close to the plane. We measure the overall radial metallicity gradient of the disk $R \geq 7$ kpc to be -0.063 ± 0.001 dex kpc^{-1}. The overall vertical metallicity gradient of the disk at

the solar neighborhood is -0.322 ± 0.01 dex kpc^{-1}. Both the radial and vertical metallicity gradients flatten with increasing stellar age.

- **Metallicity Distribution Function:** The MDF of the inner Galaxy has the widest spread, but this narrows with radius. The shape of the MDF skews strongly for the low-α disk, transitioning around $R \sim 9.4$ kpc from having a metal-poor tail in the inner Galaxy to having a metal-rich tail in the outer Galaxy.

- **Age Gradients:** Like the metallicity gradient, the age profile of the disk is flat in the inner Galaxy but transitions to a negative gradient in the outer Galaxy. The outer Galaxy's gradient is steeper at higher Z for the low-α population, and flat everywhere for the high-α stars.

- **Age Distribution Function:** The ADF for the low-α disk changes in skewness similar to the MDF, with the inner Galaxy skewed towards younger ages, and the outer Galaxy skewed towards older ages. Above the plane ($|Z| > 1$ kpc), there is significant overlap between the ADF of the low-α and high-α populations, which does not hold closer to the plane.

- **Age-Metallicity Relation:** The AMR exhibits significant spread near the solar neighborhood, but is more tightly constrained in the inner Galaxy and at larger vertical heights. The slope of the age-metallicity relation varies with radius, and there exists a population of older, metal-rich stars around the solar neighborhood that are likely present due to radial migration. The age-metallicity relation suggests that the outer disk began forming low-α stars while the high-α sequence was still forming in the inner disk.

- **Age-Alpha Relation and Chemical Clocks:** The age-alpha relation appears bimodal nearly everywhere in the Galaxy. The low-α sequence evolves significantly with Galactic position, while the high-α sequence displays a constant trend independent of Galactic position. There may be evidence of a three-phase star formation history just outside the solar neighborhood ($9 < R < 12$ kpc).

Our results suggest that radial migration is an important process in shaping the present-day appearance of the disk, especially at large radii and close to the

Galactic plane. However, stellar migration alone cannot explain the bimodal nature of the α-element abundances or the distribution of stellar ages in the disk. A non-continuous evolution model, such as the two-infall scenario or clumpy star formation, appears necessary to explain the trends seen in the inner Galaxy.

ACKNOWLEDGEMENTS

REFERENCES

Abdurro'uf, Accetta, K., Aerts, C., et al. 2022, ApJS, 259, 35, doi: 10.3847/1538-4365/ac4414

Aguirre, V. S., Bojsen-Hansen, M., Slumstrup, D., et al. 2018, Monthly Notices of the Royal Astronomical Society, doi: 10.1093/mnras/sty150

Allende Prieto, C., Beers, T. C., Wilhelm, R., et al. 2006, ApJ, 636, 804, doi: 10.1086/498131

Amarante, J. A. S., Beraldo e Silva, L., Debattista, V. P., & Smith, M. C. 2020, ApJL, 891, L30, doi: 10.3847/2041-8213/ab78a4

Amôres, E. B., Robin, A. C., & Reylé, C. 2017, A&A, 602, A67, doi: 10.1051/0004-6361/201628461

Anders, F., Chiappini, C., Santiago, B. X., et al. 2014, A&A, 564, A115, doi: 10.1051/0004-6361/201323038

Antoja, T., Ramos, P., Mateu, C., et al. 2020, A&A, 635, L3, doi: 10.1051/0004-6361/201937145

Barbanis, B., & Woltjer, L. 1967, ApJ, 150, 461, doi: 10.1086/149349

Beaton, R. L., Oelkers, R. J., Hayes, C. R., et al. 2021, The Astronomical Journal, 162, 302, doi: 10.3847/1538-3881/ac260c

Bedell, M., Bean, J. L., Meléndez, J., et al. 2018, ApJ, 865, 68, doi: 10.3847/1538-4357/aad908

Bensby, T., Feltzing, S., Lundström, I., & Ilyin, I. 2005, A&A, 433, 185, doi: 10.1051/0004-6361:20040332

Bensby, T., Feltzing, S., & Oey, M. S. 2014, A&A, 562, A71, doi: 10.1051/0004-6361/201322631

Bensby, T., Zenn, A. R., Oey, M. S., & Feltzing, S. 2007, The Astrophysical Journal, 663, L13, doi: 10.1086/519792

Beraldo e Silva, L., Debattista, V. P., Khachaturyants, T., & Nidever, D. 2020, MNRAS, 492, 4716, doi: 10.1093/mnras/staa065

Bergemann, M., Ruchti, G. R., Serenelli, A., et al. 2014, A&A, 565, A89, doi: 10.1051/0004-6361/201423456

Bilitewski, T., & Schönrich, R. 2012, Monthly Notices of the Royal Astronomical Society, 426, 2266, doi: 10.1111/j.1365-2966.2012.21827.x

Bird, J. C., Kazantzidis, S., Weinberg, D. H., et al. 2013, The Astrophysical Journal, 773, 43, doi: 10.1088/0004-637x/773/1/43

Bird, J. C., Loebman, S. R., Weinberg, D. H., et al. 2021, Monthly Notices of the Royal Astronomical Society, 503, 1815, doi: 10.1093/mnras/stab289

Bland-Hawthorn, J., & Gerhard, O. 2016, ARA&A, 54, 529, doi: 10.1146/annurev-astro-081915-023441

Blanton, M. R., Bershady, M. A., Abolfathi, B., et al. 2017, AJ, 154, 28, doi: 10.3847/1538-3881/aa7567

Boeche, C., Siebert, A., Piffl, T., et al. 2013, Astronomy &amp Astrophysics, 559, A59, doi: 10.1051/0004-6361/201322085

Bovy, J., Rix, H.-W., & Hogg, D. W. 2012a, The Astrophysical Journal, 751, 131, doi: 10.1088/0004-637x/751/2/131

Bovy, J., Rix, H.-W., Liu, C., et al. 2012b, The Astrophysical Journal, 753, 148, doi: 10.1088/0004-637x/753/2/148

Bovy, J., Rix, H.-W., Schlafly, E. F., et al. 2016, The Astrophysical Journal, 823, 30, doi: 10.3847/0004-637x/823/1/30

Bowen, I. S., & Vaughan, A. H., J 1973, ApOpt, 12, 1430, doi: 10.1364/AO.12.001430

Bregman, J. N. 1980, ApJ, 236, 577, doi: 10.1086/157776

Brook, C. B., Kawata, D., Gibson, B. K., & Freeman, K. C. 2004, ApJ, 612, 894, doi: 10.1086/422709

Buder, S., Asplund, M., Duong, L., et al. 2018, Monthly Notices of the Royal Astronomical Society, 478, 4513–4552, doi: 10.1093/mnras/sty1281

Buder, S., Lind, K., Ness, M. K., et al. 2021, Monthly Notices of the Royal Astronomical Society, 510, 2407, doi: 10.1093/mnras/stab3504

Carrell, K., Chen, Y., & Zhao, G. 2012, The Astronomical Journal, 144, 185, doi: 10.1088/0004-6256/144/6/185

Casagrande, L., Schönrich, R., Asplund, M., et al. 2011, A&A, 530, A138, doi: 10.1051/0004-6361/201016276

Casamiquela, L., Soubiran, C., Jofré , P., et al. 2021, Astronomy &amp Astrophysics, 652, A25, doi: 10.1051/0004-6361/202039951

Chen, B., Hayden, M. R., Sharma, S., et al. 2022, Chemical Evolution with Radial Mixing Redux: Extending beyond the Solar Neighborhood, arXiv, doi: 10.48550/ARXIV.2204.11413

Cheng, J. Y., Rockosi, C. M., Morrison, H. L., et al. 2012, ApJ, 746, 149, doi: 10.1088/0004-637X/746/2/149

Cheng, X., Anguiano, B., Majewski, S. R., et al. 2020, The Astrophysical Journal, 905, 49, doi: 10.3847/1538-4357/abc3c2

Chiappini, C., Matteucci, F., & Gratton, R. 1997, ApJ, 477, 765, doi: 10.1086/303726

Chiappini, C., Matteucci, F., & Romano, D. 2001, The Astrophysical Journal, 554, 1044, doi: 10.1086/321427

Choi, J., Dotter, A., Conroy, C., et al. 2016, The Astrophysical Journal, 823, 102, doi: 10.3847/0004-637x/823/2/102

Chrobáková, , Nagy, R., & López-Corredoira, M. 2022, Warp and flare of the Galactic disc revealed with supergiants by Gaia EDR3, arXiv, doi: 10.48550/ARXIV.2206.08230

Ciucă , I., Kawata, D., Miglio, A., Davies, G. R., & Grand, R. J. J. 2021, Monthly Notices of the Royal Astronomical Society, 503, 2814, doi: 10.1093/mnras/stab639

Clarke, A. J., Debattista, V. P., Nidever, D. L., et al. 2019, MNRAS, 484, 3476, doi: 10.1093/mnras/stz104

da Silva, R., Porto de Mello, G. F., Milone, A. C., et al. 2012, A&A, 542, A84, doi: 10.1051/0004-6361/201118751

Dalcanton, J. J. 2007, ApJ, 658, 941, doi: 10.1086/508913

Dias, W. S., Monteiro, H., Lé pine, J. R. D., & Barros, D. A. 2019, Monthly Notices of the Royal Astronomical Society, 486, 5726, doi: 10.1093/mnras/stz1196

Donor, J., Frinchaboy, P. M., Cunha, K., et al. 2020, AJ, 159, 199, doi: 10.3847/1538-3881/ab77bc

Edvardsson, B., Andersen, J., Gustafsson, B., et al. 1993, A&A, 275, 101

Eggen, O. J., Lynden-Bell, D., & Sandage, A. R. 1962, ApJ, 136, 748, doi: 10.1086/147433

Eilers, A.-C., Hogg, D. W., Rix, H.-W., et al. 2021, arXiv e-prints, arXiv:2112.03295. https://arxiv.org/abs/2112.03295

Elmegreen, B. G., Elmegreen, D. M., Vollbach, D. R., Foster, E. R., & Ferguson, T. E. 2005, ApJ, 634, 101, doi: 10.1086/496952

Feuillet, D. K., Frankel, N., Lind, K., et al. 2019, Monthly Notices of the Royal Astronomical Society, 489, 1742–1752, doi: 10.1093/mnras/stz2221

Feuillet, D. K., Bovy, J., Holtzman, J., et al. 2018, MNRAS, 477, 2326, doi: 10.1093/mnras/sty779

Finlator, K., & Davé , R. 2008, Monthly Notices of the Royal Astronomical Society, 385, 2181, doi: 10.1111/j.1365-2966.2008.12991.x

Frankel, N., Rix, H.-W., Ting, Y.-S., Ness, M., & Hogg, D. W. 2018, The Astrophysical Journal, 865, 96, doi: 10.3847/1538-4357/aadba5

Frankel, N., Sanders, J., Rix, H.-W., Ting, Y.-S., & Ness, M. 2019, ApJ, 884, 99, doi: 10.3847/1538-4357/ab4254

Frankel, N., Sanders, J., (), Y.-S. T., & Rix, H.-W. 2020, The Astrophysical Journal, 896, 15, doi: 10.3847/1538-4357/ab910c

Fraternali, F. 2017, in Astrophysics and Space Science Library, Vol. 430, Gas Accretion onto Galaxies, ed. A. Fox & R. Davé, 323, doi: 10.1007/978-3-319-52512-9_14

Freudenburg, J. K. C., Weinberg, D. H., Hayden, M. R., & Holtzman, J. A. 2017, The Astrophysical Journal, 849, 17, doi: 10.3847/1538-4357/aa8c03

Fuhrmann, K. 1998, A&A, 338, 161

Gaia Collaboration, Brown, A. G. A., Vallenari, A., et al. 2018, A&A, 616, A1, doi: 10.1051/0004-6361/201833051

—. 2021, A&A, 650, C3, doi: 10.1051/0004-6361/202039657e

Gaia Collaboration, Recio-Blanco, A., Kordopatis, G., et al. 2022, Gaia Data Release 3: Chemical cartography of the Milky Way. https://arxiv.org/abs/2206.05534

García Pérez, A. E., Allende Prieto, C., Holtzman, J. A., et al. 2016, AJ, 151, 144, doi: 10.3847/0004-6256/151/6/144

Genovali, K., Lemasle, B., Bono, G., et al. 2014, A&A, 566, A37, doi: 10.1051/0004-6361/201323198

Gibson, B. K., Pilkington, K., Brook, C. B., Stinson, G. S., & Bailin, J. 2013, Astronomy &amp Astrophysics, 554, A47, doi: 10.1051/0004-6361/201321239

Gilmore, G., & Reid, N. 1983, MNRAS, 202, 1025, doi: 10.1093/mnras/202.4.1025

Gilmore, G., Randich, S., Worley, C. C., et al. 2022, The Gaia-ESO Public Spectroscopic Survey: Motivation, implementation, GIRAFFE data processing, analysis, and final data products, arXiv, doi: 10.48550/ARXIV.2208.05432

Grieves, N., Ge, J., Thomas, N., et al. 2018, Monthly Notices of the Royal Astronomical Society, 481, 3244, doi: 10.1093/mnras/sty2431

Gunn, J. E., Siegmund, W. A., Mannery, E. J., et al. 2006, AJ, 131, 2332, doi: 10.1086/500975

Guo, Y., Ferguson, H. C., Bell, E. F., et al. 2015, The Astrophysical Journal, 800, 39, doi: 10.1088/0004-637x/800/1/39

Halle, A., Matteo, P. D., Haywood, M., & Combes, F. 2015, Astronomy &amp Astrophysics, 578, A58, doi: 10.1051/0004-6361/201525612

Hartkopf, W. I., & Yoss, K. M. 1982, AJ, 87, 1679, doi: 10.1086/113261

Hasselquist, S., Holtzman, J. A., Shetrone, M., et al. 2019, The Astrophysical Journal, 871, 181, doi: 10.3847/1538-4357/aaf859

Hasselquist, S., Zasowski, G., Feuillet, D. K., et al. 2020, The Astrophysical Journal, 901, 109, doi: 10.3847/1538-4357/abaeee

Hawkins, K. 2022, Chemical Cartography with LAMOST and Gaia Reveal Azimuthal and Spiral Structure in the Galactic Disk, arXiv, doi: 10.48550/ARXIV.2207.04542

Hawkins, K., Jofré, P., Masseron, T., & Gilmore, G. 2015, Monthly Notices of the Royal Astronomical Society, 453, 758, doi: 10.1093/mnras/stv1586

Hayden, M. R., Recio-Blanco, A., de Laverny, P., Mikolaitis, S., & Worley, C. C. 2017, Astronomy &amp Astrophysics, 608, L1, doi: 10.1051/0004-6361/201731494

Hayden, M. R., Holtzman, J. A., Bovy, J., et al. 2014, AJ, 147, 116, doi: 10.1088/0004-6256/147/5/116

Hayden, M. R., Bovy, J., Holtzman, J. A., et al. 2015, The Astrophysical Journal, 808, 132, doi: 10.1088/0004-637x/808/2/132

Hayden, M. R., Sharma, S., Bland-Hawthorn, J., et al. 2020, The GALAH Survey: Chemical Clocks, arXiv, doi: 10.48550/ARXIV.2011.13745

Haywood, M., Lehnert, M. D., Matteo, P. D., et al. 2016, Astronomy &amp Astrophysics, 589, A66, doi: 10.1051/0004-6361/201527567

Haywood, M., Matteo, P. D., Lehnert, M., et al. 2018, Astronomy &amp Astrophysics, 618, A78, doi: 10.1051/0004-6361/201731363

Haywood, M., Matteo, P. D., Lehnert, M. D., Katz, D., & Gó mez, A. 2013, Astronomy &amp Astrophysics, 560, A109, doi: 10.1051/0004-6361/201321397

Haywood, M., Snaith, O., Lehnert, M. D., Matteo, P. D., & Khoperskov, S. 2019, Astronomy &amp Astrophysics, 625, A105, doi: 10.1051/0004-6361/201834155

Helmi, A., Babusiaux, C., Koppelman, H. H., et al. 2018, Nature, 563, 85, doi: 10.1038/s41586-018-0625-x

Holtzman, J. A., Shetrone, M., Johnson, J. A., et al. 2015, AJ, 150, 148, doi: 10.1088/0004-6256/150/5/148

Holtzman, J. A., Hasselquist, S., Shetrone, M., et al. 2018, The Astronomical Journal, 156, 125, doi: 10.3847/1538-3881/aad4f9

Huang, Y., Schönrich, R., Zhang, H., et al. 2020, The Astrophysical Journal Supplement Series, 249, 29, doi: 10.3847/1538-4365/ab994f

Hänninen, J., & Flynn, C. 2002, Monthly Notices of the Royal Astronomical Society, 337, 731, doi: 10.1046/j.1365-8711.2002.05956.x

Inno, L., Urbaneja, M. A., Matsunaga, N., et al. 2019, MNRAS, 482, 83, doi: 10.1093/mnras/sty2661

Isern, J. 2019, The Astrophysical Journal, 878, L11, doi: 10.3847/2041-8213/ab238e

Johnson, J. W., Weinberg, D. H., Vincenzo, F., et al. 2021, Monthly Notices of the Royal Astronomical Society, 508, 4484, doi: 10.1093/mnras/stab2718

Jurić, M., Ivezić, Ž., Brooks, A., et al. 2008, ApJ, 673, 864, doi: 10.1086/523619

Jönsson, H., Prieto, C. A., Holtzman, J. A., et al. 2018, The Astronomical Journal, 156, 126, doi: 10.3847/1538-3881/aad4f5

Jönsson, H., Holtzman, J. A., Prieto, C. A., et al. 2020, The Astronomical Journal, 160, 120, doi: 10.3847/1538-3881/aba592

Katz, D., Gó mez, A., Haywood, M., Snaith, O., & Matteo, P. D. 2021, Astronomy &amp Astrophysics, 655, A111, doi: 10.1051/0004-6361/202140453

Kawata, D., & Chiappini, C. 2016, Astronomische Nachrichten, 337, 976, doi: 10.1002/asna.201612421

Khoperskov, S., Gerhard, O., Matteo, P. D., et al. 2020a, Astronomy &amp Astrophysics, 634, L8, doi: 10.1051/0004-6361/201936645

Khoperskov, S., Haywood, M., Snaith, O., et al. 2021, MNRAS, 501, 5176, doi: 10.1093/mnras/staa3996

Khoperskov, S., Matteo, P. D., Haywood, M., Gó mez, A., & Snaith, O. N. 2020b, Astronomy &amp Astrophysics, 638, A144, doi: 10.1051/0004-6361/201937188

Kobayashi, C., & Nakasato, N. 2011, ApJ, 729, 16, doi: 10.1088/0004-637X/729/1/16

Kordopatis, G., Gilmore, G., Wyse, R. F. G., et al. 2013, MNRAS, 436, 3231, doi: 10.1093/mnras/stt1804

Kubryk, M., Prantzos, N., & Athanassoula, E. 2015, Astronomy &amp Astrophysics, 580, A126, doi: 10.1051/0004-6361/201424171

Lacey, C. G. 1984, MNRAS, 208, 687, doi: 10.1093/mnras/208.4.687

Laporte, C. F. P., Minchev, I., Johnston, K. V., & Gómez, F. A. 2019, MNRAS, 485, 3134, doi: 10.1093/mnras/stz583

Larson, R. B. 1976, MNRAS, 176, 31, doi: 10.1093/mnras/176.1.31

Lee, Y. S., Beers, T. C., An, D., et al. 2011, ApJ, 738, 187, doi: 10.1088/0004-637X/738/2/187

Lemasle, B., Hajdu, G., Kovtyukh, V., et al. 2018, Astronomy &amp Astrophysics, 618, A160, doi: 10.1051/0004-6361/201834050

Leung, H. W., & Bovy, J. 2018, Monthly Notices of the Royal Astronomical Society, doi: 10.1093/mnras/sty3217

Lian, J., Thomas, D., Maraston, C., et al. 2020a, Monthly Notices of the Royal Astronomical Society, 494, 2561, doi: 10.1093/mnras/staa867

—. 2020b, Monthly Notices of the Royal Astronomical Society, 497, 2371–2384, doi: 10.1093/mnras/staa2078

Lian, J., Zasowski, G., Hasselquist, S., et al. 2020c, Monthly Notices of the Royal Astronomical Society, 497, 3557, doi: 10.1093/mnras/staa2205

Lian, J., Zasowski, G., Hasselquist, S., et al. 2021, MNRAS, 500, 282, doi: 10.1093/mnras/staa3256

Lian, J., Zasowski, G., Mackereth, T., et al. 2022a, Monthly Notices of the Royal Astronomical Society, 513, 4130, doi: 10.1093/mnras/stac1151

Lian, J., Zasowski, G., Hasselquist, S., et al. 2022b, Monthly Notices of the Royal Astronomical Society, 511, 5639–5655, doi: 10.1093/mnras/stac479

Lin, J., Dotter, A., Ting, Y.-S., & Asplund, M. 2018, MNRAS, 477, 2966, doi: 10.1093/mnras/sty709

Lin, J., Asplund, M., Ting, Y.-S., et al. 2019, Monthly Notices of the Royal Astronomical Society, 491, 2043, doi: 10.1093/mnras/stz3048

Linden, S. T., Pryal, M., Hayes, C. R., et al. 2017, ApJ, 842, 49, doi: 10.3847/1538-4357/aa6f17

Loebman, S. R., Debattista, V. P., Nidever, D. L., et al. 2016, The Astrophysical Journal, 818, L6, doi: 10.3847/2041-8205/818/1/l6

Lu, Y. L., Ness, M. K., Buck, T., & Carr, C. 2022, MNRAS, 512, 4697, doi: 10.1093/mnras/stac780

Luo, A.-L., Zhao, Y.-H., Zhao, G., et al. 2015, Research in Astronomy and Astrophysics, 15, 1095–1124, doi: 10.1088/1674-4527/15/8/002

Mackereth, J. T., Crain, R. A., Schiavon, R. P., et al. 2018, Monthly Notices of the Royal Astronomical Society, 477, 5072, doi: 10.1093/mnras/sty972

Mackereth, J. T., Bovy, J., Schiavon, R. P., et al. 2017, MNRAS, 471, 3057, doi: 10.1093/mnras/stx1774

Mackereth, J. T., Bovy, J., Leung, H. W., et al. 2019, MNRAS, 489, 176, doi: 10.1093/mnras/stz1521

Magrini, L., Coccato, L., Stanghellini, L., Casasola, V., & Galli, D. 2016, Astronomy &amp Astrophysics, 588, A91, doi: 10.1051/0004-6361/201527799

Magrini, L., Vincenzo, F., Randich, S., et al. 2018, Astronomy &amp Astrophysics, 618, A102, doi: 10.1051/0004-6361/201833224

Majewski, S. R., Schiavon, R. P., Frinchaboy, P. M., et al. 2017, AJ, 154, 94, doi: 10.3847/1538-3881/aa784d

Marinacci, F., Fraternali, F., Nipoti, C., et al. 2011, MNRAS, 415, 1534, doi: 10.1111/j.1365-2966.2011.18810.x

Matteucci, F., & Brocato, E. 1990, ApJ, 365, 539, doi: 10.1086/169508

Matteucci, F., & Francois, P. 1989, MNRAS, 239, 885, doi: 10.1093/mnras/239.3.885

Mészáros, S., Allende Prieto, C., Edvardsson, B., et al. 2012, AJ, 144, 120, doi: 10.1088/0004-6256/144/4/120

Michtchenko, T. A., Vieira, R. S. S., Barros, D. A., & Lé pine, J. R. D. 2016, Astronomy &amp Astrophysics, 597, A39, doi: 10.1051/0004-6361/201628895

Miglio, A., Chiappini, C., Mackereth, J. T., et al. 2021, Astronomy &amp Astrophysics, 645, A85, doi: 10.1051/0004-6361/202038307

Minchev, I., Chiappini, C., & Martig, M. 2013, Astronomy &amp Astrophysics, 558, A9, doi: 10.1051/0004-6361/201220189

—. 2014, Astronomy &amp Astrophysics, 572, A92, doi: 10.1051/0004-6361/201423487

Minchev, I., Martig, M., Streich, D., et al. 2015, ApJL, 804, L9, doi: 10.1088/2041-8205/804/1/L9

Minchev, I., Steinmetz, M., Chiappini, C., et al. 2017, ApJ, 834, 27, doi: 10.3847/1538-4357/834/1/27

Minchev, I., Anders, F., Recio-Blanco, A., et al. 2018, MNRAS, 481, 1645, doi: 10.1093/mnras/sty2033

Mollá , M., Díaz, Á. I., Cavichia, O., et al. 2018, Monthly Notices of the Royal Astronomical Society, doi: 10.1093/mnras/sty2877

Mor, R., Robin, A. C., Figueras, F., Roca-Fàbrega, S., & Luri, X. 2019, A&A, 624, L1, doi: 10.1051/0004-6361/201935105

Myers, N., Donor, J., Spoo, T., et al. 2022, AJ, 164, 85, doi: 10.3847/1538-3881/ac7ce5

Ness, M., Hogg, D. W., Rix, H. W., et al. 2016, ApJ, 823, 114, doi: 10.3847/0004-637X/823/2/114

Nidever, D. L., Bovy, J., Bird, J. C., et al. 2014, ApJ, 796, 38, doi: 10.1088/0004-637X/796/1/38

Nidever, D. L., Holtzman, J. A., Allende Prieto, C., et al. 2015, AJ, 150, 173, doi: 10.1088/0004-6256/150/6/173

Nissen, P. E. 2015, A&A, 579, A52, doi: 10.1051/0004-6361/201526269

Pilkington, K., & Gibson, B. K. 2012, Metallicity Gradients in Simulated Disk Galaxies, arXiv, doi: 10.48550/ARXIV.1201.6417

Pinsonneault, M. H., Elsworth, Y. P., Tayar, J., et al. 2018, The Astrophysical Journal Supplement Series, 239, 32, doi: 10.3847/1538-4365/aaebfd

Poggio, E., Recio-Blanco, A., Palicio, P. A., et al. 2022, The chemical signature of the Galactic spiral arms revealed by Gaia DR3, arXiv, doi: 10.48550/ARXIV.2206.14849

Price-Jones, N., Bovy, J., Webb, J. J., et al. 2020, Monthly Notices of the Royal Astronomical Society, 496, 5101, doi: 10.1093/mnras/staa1905

Queiroz, A. B. A., Chiappini, C., Perez-Villegas, A., et al. 2021, A&A, 656, A156, doi: 10.1051/0004-6361/202039030

Quinn, P. J., Hernquist, L., & Fullagar, D. P. 1993, ApJ, 403, 74, doi: 10.1086/172184

Rahimi, A., Carrell, K., & Kawata, D. 2014, Research in Astronomy and Astrophysics, 14, 1406, doi: 10.1088/1674-4527/14/11/004

Reddy, B. E., Lambert, D. L., & Prieto, C. A. 2006, Monthly Notices of the Royal Astronomical Society, 367, 1329–1366, doi: 10.1111/j.1365-2966.2006.10148.x

Reid, M. J., Menten, K. M., Brunthaler, A., et al. 2019, ApJ, 885, 131, doi: 10.3847/1538-4357/ab4a11

Robin, A. C., Bienaymé , O., Fernández-Trincado, J. G., & Reylé, C. 2017, Astronomy &amp Astrophysics, 605, A1, doi: 10.1051/0004-6361/201630217

Robin, A. C., Bienaymé, O., Salomon, J. B., et al. 2022, arXiv e-prints, arXiv:2208.13827. https://arxiv.org/abs/2208.13827

Romano, D., & Starkenburg, E. 2013, Monthly Notices of the Royal Astronomical Society, 434, 471, doi: 10.1093/mnras/stt1033

Roškar, R., Debattista, V. P., Quinn, T. R., Stinson, G. S., & Wadsley, J. 2008, ApJL, 684, L79, doi: 10.1086/592231

Ruiz-Lara, T., Gallart, C., Bernard, E. J., & Cassisi, S. 2020, Nature Astronomy, 4, 965, doi: 10.1038/s41550-020-1097-0

Sahlholdt, C. L., Feltzing, S., & Feuillet, D. K. 2022, MNRAS, 510, 4669, doi: 10.1093/mnras/stab3681

Santana, F. A., Beaton, R. L., Covey, K. R., et al. 2021, The Astronomical Journal, 162, 303, doi: 10.3847/1538-3881/ac2cbc

Schlesinger, K. J., Johnson, J. A., Rockosi, C. M., et al. 2014, ApJ, 791, 112, doi: 10.1088/0004-637X/791/2/112

Schönrich, R., & Binney, J. 2009a, MNRAS, 396, 203, doi: 10.1111/j.1365-2966.2009.14750.x

—. 2009b, Monthly Notices of the Royal Astronomical Society, 399, 1145, doi: 10.1111/j.1365-2966.2009.15365.x

Sellwood, J. A., & Binney, J. J. 2002, MNRAS, 336, 785, doi: 10.1046/j.1365-8711.2002.05806.x

Shapiro, P. R., & Field, G. B. 1976, ApJ, 205, 762, doi: 10.1086/154332

Sharma, S., Hayden, M. R., & Bland-Hawthorn, J. 2021a, Monthly Notices of the Royal Astronomical Society, 507, 5882, doi: 10.1093/mnras/stab2015

Sharma, S., Hayden, M. R., Bland-Hawthorn, J., et al. 2021b, Monthly Notices of the Royal Astronomical Society, 510, 734, doi: 10.1093/mnras/stab3341

Shetrone, M., Bizyaev, D., Lawler, J. E., et al. 2015, ApJS, 221, 24, doi: 10.1088/0067-0049/221/2/24

Smith, V. V., Bizyaev, D., Cunha, K., et al. 2021, AJ, 161, 254, doi: 10.3847/1538-3881/abefdc

Soubiran, C., Bienaymé, O., & Siebert, A. 2003, A&A, 398, 141, doi: 10.1051/0004-6361:20021615

Spitoni, E., Aguirre, V. S., Matteucci, F., Calura, F., & Grisoni, V. 2019a, Astronomy &amp Astrophysics, 623, A60, doi: 10.1051/0004-6361/201834188

Spitoni, E., Børsen-Koch, V. A., Verma, K., & Stokholm, A. 2022a, Astronomy &amp Astrophysics, 663, A174, doi: 10.1051/0004-6361/202142469

Spitoni, E., Cescutti, G., Minchev, I., et al. 2019b, Astronomy &amp Astrophysics, 628, A38, doi: 10.1051/0004-6361/201834665

Spitoni, E., Verma, K., Aguirre, V. S., & Calura, F. 2020, Astronomy &amp Astrophysics, 635, A58, doi: 10.1051/0004-6361/201937275

Spitoni, E., Verma, K., Aguirre, V. S., et al. 2021,
  Astronomy &amp Astrophysics, 647, A73,
  doi: 10.1051/0004-6361/202039864

Spitoni, E., Recio-Blanco, A., de Laverny, P., et al. 2022b,
  Beyond the two-infall model with Gaia DR3 -element
  abundances, arXiv, doi: 10.48550/ARXIV.2206.12436

Spitzer, Lyman, J., & Schwarzschild, M. 1951, ApJ, 114,
  385, doi: 10.1086/145478

Steinmetz, M., Matijevič, G., Enke, H., et al. 2020, AJ, 160,
  82, doi: 10.3847/1538-3881/ab9ab9

Thomas, D., Maraston, C., Bender, R., & Mendes de
  Oliveira, C. 2005, ApJ, 621, 673, doi: 10.1086/426932

Ting, Y.-S., Conroy, C., & Rix, H.-W. 2015, The
  Astrophysical Journal, 816, 10,
  doi: 10.3847/0004-637x/816/1/10

Toth, G., & Ostriker, J. P. 1992, ApJ, 389, 5,
  doi: 10.1086/171185

Toyouchi, D., & Chiba, M. 2018, ApJ, 855, 104,
  doi: 10.3847/1538-4357/aab044

Twarog, B. A. 1980, ApJ, 242, 242, doi: 10.1086/158460

Vázquez, C. V., Magrini, L., Casali, G., et al. 2022,
  Astronomy &amp Astrophysics, 660, A135,
  doi: 10.1051/0004-6361/202142937

Vickers, J. J., Shen, J., & Li, Z.-Y. 2021, The Astrophysical
  Journal, 922, 189, doi: 10.3847/1538-4357/ac27a9

Vincenzo, F., Matteucci, F., Vattakunnel, S., & Lanfranchi,
  G. A. 2014, Monthly Notices of the Royal Astronomical
  Society, 441, 2815, doi: 10.1093/mnras/stu710

Vincenzo, F., Spitoni, E., Calura, F., et al. 2019, Monthly
  Notices of the Royal Astronomical Society: Letters, 487,
  L47, doi: 10.1093/mnrasl/slz070

Vincenzo, F., Weinberg, D. H., Miglio, A., Lane, R. R., &
  Roman-Lopes, A. 2021, Monthly Notices of the Royal
  Astronomical Society, 508, 5903–5920,
  doi: 10.1093/mnras/stab2899

Wang, Y., & Zhao, G. 2013, The Astrophysical Journal,
  769, 4, doi: 10.1088/0004-637x/769/1/4

Wegg, C., Rojas-Arriagada, A., Schultheis, M., & Gerhard,
  O. 2019, Astronomy &amp Astrophysics, 632, A121,
  doi: 10.1051/0004-6361/201936779

Weinberg, D. H., Andrews, B. H., & Freudenburg, J. 2017,
  ApJ, 837, 183, doi: 10.3847/1538-4357/837/2/183

Weinberg, D. H., Holtzman, J. A., Hasselquist, S., et al.
  2019, The Astrophysical Journal, 874, 102,
  doi: 10.3847/1538-4357/ab07c7

Weinberg, D. H., Holtzman, J. A., Johnson, J. A., et al.
  2022, The Astrophysical Journal Supplement Series, 260,
  32, doi: 10.3847/1538-4365/ac6028

Wenger, T. V., Balser, D. S., Anderson, L. D., & Bania,
  T. M. 2019, ApJ, 887, 114,
  doi: 10.3847/1538-4357/ab53d3

Wilson, J. C., Hearty, F. R., Skrutskie, M. F., et al. 2019,
  PASP, 131, 055001, doi: 10.1088/1538-3873/ab0075

Wu, Y., Xiang, M., Zhao, G., et al. 2019, Monthly Notices
  of the Royal Astronomical Society, 484, 5315,
  doi: 10.1093/mnras/stz256

Xiang, M., & Rix, H.-W. 2022, Nature, 603, 599,
  doi: 10.1038/s41586-022-04496-5

Yoshii, Y. 1982, PASJ, 34, 365

Zamora, O., García-Hernández, D. A., Allende Prieto, C.,
  et al. 2015, AJ, 149, 181,
  doi: 10.1088/0004-6256/149/6/181

Zasowski, G., Johnson, J. A., Frinchaboy, P. M., et al.
  2013, AJ, 146, 81, doi: 10.1088/0004-6256/146/4/81

Zasowski, G., Cohen, R. E., Chojnowski, S. D., et al. 2017,
  AJ, 154, 198, doi: 10.3847/1538-3881/aa8df9

Zasowski, G., Schultheis, M., Hasselquist, S., et al. 2019,
  ApJ, 870, 138, doi: 10.3847/1538-4357/aaeff4